Path integral simulations of rotors: theory and applications

1999 J. Phys.: Condens. Matter 11 R117

(http://iopscience.iop.org/0953-8984/11/11/003)

J. Phys.: Condens. Matter **11** (1999) R117–R155. Printed in the UK PII: S0953-8984(99)67859-6

REVIEW ARTICLE

Path integral simulations of rotors: theory and applications

Dominik Marx† and Martin H Müser‡§

† Max-Planck-Institut für Festkörperforschung, Heisenbergstrasse 1, 70569 Stuttgart, Germany
‡ Department of Physics and Astronomy, Johns Hopkins University, Baltimore, MD 21218, USA

Received 13 November 1998

Abstract. An outline of numerical path integral techniques which allows one to treat the rotational component of molecular motion is given in a unified framework. Special attention is paid to the particular aspects of this treatment depending on the dimension of the subspace for rotations, which leads to optimized methods for one-, two- and three-dimensional rigid rotors. The implications of the coupling between rotational and nuclear spin degrees of freedom, due to the symmetry requirement of the total wave function under exchange of identical particles, are discussed. Several recent applications of path integral simulations of rigid rotors are presented. These examples include both strongly simplified and very realistic models for investigating the properties of molecular impurities and clusters, rotors physisorbed on surfaces, and condensed molecular phases. Where available, the results of approximate calculations based on quasi-classical, quasi-harmonic and mean-field theories are compared to the path integral simulations.

Contents

1. Preliminary remarks
2. Path integral techniques for rotations
   2.1. General remarks
   2.2. One-dimensional rotation
   2.3. Two-dimensional rotation
   2.4. Three-dimensional rotation
   2.5. Coupling to nuclear spins
3. Selected applications
   3.1. Rotor impurities
   3.2. Rotors on surfaces
   3.3. Rotors in the bulk
4. Concluding remarks

1. Preliminary remarks

The investigation of quantum many-body systems at finite temperatures is a notoriously difficult task. A powerful arsenal of sophisticated methods exist to tackle quantum many-body problems in an approximate way, e.g., mean-field, quasi-classical, infinite-dimension, reduced-dimensionality, etc theories. Another approach is to start out by using simplified models which can be solved exactly. The philosophy of quantum simulations is a third route [19]. The

§ Present address: Institut für Physik, Johannes Gutenberg-Universität, 55099 Mainz, Germany.

0953-8984/99/110117+39$19.50

fundamental idea of computer simulations is to 'solve' a well-defined many-body Hamiltonian that is 'numerically exact'. In this context, to 'solve' means that any (equilibrium) observable can be calculated in principle. 'Numerically exact' means that observables are calculated within statistical error bars and no uncontrollable approximations are employed. Ideally, statistical error bars can be determined in the simulation and controllable errors such as finite-size corrections or finite (imaginary) time steps are kept arbitrarily small. Specifically, the purpose of path integral methods is to include the quantum fluctuations *rigorously* in the computer simulation. Pioneering path integral Monte Carlo work dates back to the sixties [41, 42, 69], and the basic philosophy is still valid today: 'This technique involves first, an approximation of the Wiener integral by an n-dimensional integral and, second, a Monte Carlo estimation of the value of the n-dimensional integral' [41]. The major breakthrough of path integral methods started, however, only in the early eighties [3, 6, 26, 104, 149, 151].

Path integral simulations are now recognized as very powerful tools in investigating off-lattice many-body quantum systems at finite temperatures. Here, 'many' means of the order of 100 or in some cases even 1000 atoms or molecules [76, 88], and 'finite temperatures' encompasses the range from the order of 10^5 K [82, 122] down to the nK regime [76]. Most of the numerical applications of path integrals are based on discretizing the full kinetic energy in Cartesian coordinates. In the case of rotating molecules, however, it can be very advantageous to keep the vibrations frozen and to treat the molecules as rigid entities. This allows for the separation of the rotational kinetic energy from that associated with the centre-of-mass motion. The physical reason for this is that intramolecular vibrations are in many cases sufficiently decoupled from translations and rotations. In addition, intramolecular vibrations are not always of central interest, in particular when it comes to condensed phase phenomena. On the contrary, it is often desired to decouple the effects of rotations from those of the translations and vibrations. This allows one to separate the influence of different degrees of freedom and thus different contributions to a physical phenomenon in complex systems such as molecular crystals. It should also be mentioned that accurate flexible molecular models which include vibrations are still quite rare, so rigid models are often the only possibility for dealing with molecules. In some cases, one can use *ab initio* path integral techniques to solve this dilemma by computing the interactions directly from concurrent electronic structure calculations [5, 95, 96, 99, 159].

The main advantages of treating molecules as rigid units, however, are of a technical nature. Using rigid-molecule models, systematic and statistical errors may be reduced by orders of magnitude for given CPU time and memory. Rotational motion of molecules typically becomes quantum mechanical at much lower temperatures than intramolecular vibrations. Hence much smaller Trotter numbers are needed in simulations of rigid-molecule models than in simulations of fully flexible models typically carried out in Cartesian coordinates. In addition, considerably larger Monte Carlo displacements or longer molecular dynamics time steps are possible, which further improves the sampling. Lastly, the number of active degrees of freedom is reduced, which gives an additional speeding up of the simulation. These advantages of rigid-molecule models are particularly important for many-rotor systems. Studying few rotors in a bath of point atoms makes the aforementioned advantages of fixed-rotor models less striking. Along these lines, studying phase transitions in molecular crystals or molecular adsorbates including finite-size scaling became possible; see section 3 for examples.

The development of numerical path integral techniques for rigid rotors started in the mid-eighties, shortly after an explosion of path integral simulation work at the beginning of the eighties. More recently, this field received a renewed impetus driven mainly by questions revolving around orientational phase transitions in solid molecular hydrogen and in molecular adsorbates. The path integral methods for rigid rotors have much in common with those

for translational motion, but they are nevertheless sufficiently different to call for separate attention. The purpose of the present review is to discuss path integral techniques for rigid rotors with one, two, and three rotational degrees of freedom in a unified framework. The usefulness of these methods is demonstrated by including some selected applications.

The present review focuses on the generic aspects of treating rigid-body quantum rotation within the path integral approach numerically. Thus, we have to rely on basic knowledge of path integral theory [39,40,75,137], standard path integral simulation techniques [21, 25, 35, 52, 135, 160], and Monte Carlo and molecular dynamics sampling [1, 9, 10]. Approximate treatments of rotational motion are not among the central issues covered. An extensive review on how to compute small quantum corrections to rotational motion can be found in [47]. Quantum localization phenomena in orientation space are discussed in [129].

The remainder of this review is organized as follows. We present in section 2 the theory required for solving the path integrals for rotational motion numerically. The first subsection sets the stage for what follows by showing how to decompose the density matrix into translational, rotational, and interaction contributions. Subsections 2.2, 2.3, and 2.4 deal with the specifics of one-, two-, and three-dimensional rotational degrees of freedom, respectively. The theory section is closed in subsection 2.5 by a discussion of the influence of the nuclear spin statistics on the symmetry of the rotational density matrix. A few selected applications of path integral simulations of rigid rotors are compiled in section 3. We proceed from molecular impurities and clusters presented in subsection 3.1, via rotors physisorbed on surfaces in subsection 3.2, finally to condensed molecular phases in subsection 3.3. We are well aware that this choice is biased by our own research interests. But rather than exhaustively cover all available studies, we prefer to discuss just a few showcase examples, in order to highlight some interesting aspects of path integral simulations performed in the space of rotations.

The following abbreviations are frequently used: DMC: diffusion Monte Carlo; EQQ: electric quadrupole–quadrupole; MFT: mean-field theory; PIMC: path integral Monte Carlo; PIMD: path integral molecular dynamics; QAPR: quantum anisotropic planar rotor.

2. Path integral techniques for rotations

2.1. General remarks

Throughout this review we consider N-particle systems that can be described by Hamiltonians $\hat{H}$ of the form

$$\hat{H} = \hat{T}^{\mathrm{tra}} + \hat{T}^{\mathrm{rot}} + \hat{V} \tag{2.1}$$

where $\hat{V}$ establishes among other couplings the coupling between translational and orientational degrees of freedom. In addition, we assume that the molecules are strictly approximated as rotating *rigid* bodies. Thus, two effects induced by flexibility of the rotor are neglected [164]: (i) centrifugal distortion, i.e., the variation of the molecular moment of inertia Θ with rotational quantum number due to a deformation of the molecule for high rotational excitations; and (ii) Coriolis interactions or rotational–vibrational coupling, i.e., the change of Θ as a function of the vibrational quantum number. These neglected effects are usually small in condensed phase environments, which is the main application field of the PIMC technique for rotations and is thus the focus of this review. Here, we merely refer the reader to [36,121] for early approaches to treating non-rigid (vibrating) rotors by means of path integrals in polar coordinates, to [18] for a corresponding PIMC simulation technique, and to [75] for a thorough discussion of the implications of the singularities involved .

For the sake of simplicity we assume for a moment that the system consists of one molecule only. In (2.1), the term $\hat{T}^{\mathrm{tra}}$ denotes the operator of the kinetic energy associated with the

molecule's centre-of-mass motion in a d-dimensional space, $\hat{V}$ is the potential energy of the molecule, and $\hat{T}^{\mathrm{rot}}$ is the operator of the kinetic energy associated with the d^{rot} rotational degrees of freedom. The operator T^{rot} can generally be expressed as

$$T^{\mathrm{rot}} = \sum_{i=1}^{d^{\mathrm{rot}}} \frac{\hat{L}_i^2}{2\Theta_{ii}} \tag{2.2}$$

with the $\hat{L}_i$ the components of the angular momentum operator and Θ_{ii} the moment(s) of inertia of the rigid molecule. For $d_{\mathrm{rot}} = 3$, equation (2.2) usually has to be taken in the molecule-fixed principal-axis system.

The dimension d^{rot} also corresponds to the number of coordinates needed to specify the orientation of a molecule. For a linear molecule or a flat large molecule confined to rotating in a plane, we have $d^{\mathrm{rot}} = 1$. Experimental realizations of such a situation are physisorbed N_2 or benzene C_6H_6 on a smooth substrate such as graphite or boron nitride, BN; see [98]. This type of motion will subsequently be referred to as one-dimensional rotation. The rotation of a linear molecule in $d = 3$ spatial dimensions and of an arbitrary molecule in $d = 3$ dimensions will be called two-dimensional $d^{\mathrm{rot}} = 2$ rotation and three-dimensional $d^{\mathrm{rot}} = 3$ rotation, respectively. Examples showing $d^{\mathrm{rot}} = 2$ rotation include various phases of solid H_2 [139], whereas solid methane CH_4 [66, 128] is a prototype system for showing $d^{\mathrm{rot}} = 3$ rotation. In the case of two-dimensional rotation, the two moments of inertia are identical, whereas in the case of three-dimensional rotation the various values for Θ_{ii} may differ.

The quantum mechanical partition function $Z(\beta)$ at inverse temperature $\beta = 1/k_{\mathrm{B}}T$ is given as usual as the trace of the density operator $\hat{\rho}(\beta) = \exp[-\beta\hat{H}]$:

$$Z(\beta) = \mathrm{Tr}\,\hat{\rho}(\beta) \tag{2.3}$$

and thermal expectation values of the observables $\hat{O}$ can be calculated using

$$\langle\hat{O}\rangle = \frac{1}{Z(\beta)}\mathrm{Tr}\left\{\hat{O}\hat{\rho}(\beta)\right\}. \tag{2.4}$$

Unlike the classical density function, $\hat{\rho}(\beta)$ is not diagonal in coordinate space, because position and momentum operators, and thus the potential energy and kinetic energy, do not commute. Using the semi-group property of the density matrix

$$\hat{\rho}(\beta) = \prod_{t=1}^{P} \hat{\rho}(\beta/P) \tag{2.5}$$

and the Trotter product formula [150, 153, 157] (see also [75, 137]) applied to the high-temperature density matrix $\hat{\rho}(\beta/P)$:

$$\hat{\rho}(\beta/P) = \exp\left[-\beta\hat{V}/2P\right]\exp\left[-\beta(\hat{T}^{\mathrm{kin}} + \hat{T}^{\mathrm{rot}})/P\right]\exp\left[-\beta\hat{V}/2P\right] + \mathcal{O}\left\{(\beta/P)^3\right\} \tag{2.6}$$

it is possible to map the quantum mechanical problem onto an equivalent higher-dimensional classical problem. This mapping is free of systematic errors, since the underlying Trotter theorem ensures that

$$\hat{\rho}(\beta) = \exp\left[-\beta(\hat{T}^{\mathrm{tra}} + \hat{T}^{\mathrm{rot}} + \hat{V})\right] \tag{2.7}$$

$$= \lim_{P\to\infty}\left\{\exp\left[-\beta\hat{V}/2P\right]\exp\left[-\beta(\hat{T}^{\mathrm{kin}} + \hat{T}^{\mathrm{rot}})/P\right]\exp\left[-\beta\hat{V}/2P\right]\right\}^P \tag{2.8}$$

for well-behaved potentials [75]. The mapping is achieved by substituting (2.6) into (2.5) and inserting identities $\mathbf{1}_t$ in the coordinate representation at each Trotter slice or imaginary time $t = 1, 2, \ldots, P$:

$$\mathbf{1}_t = \int \mathrm{d}\boldsymbol{r}_t \int \mathrm{d}\omega_t\, |\boldsymbol{r}_t\omega_t\rangle\langle\boldsymbol{r}_t\omega_t|. \tag{2.9}$$

Here, $\boldsymbol{r}_t$ denotes the molecule's centre-of-mass coordinates in the d-dimensional space of the translations and ω_t stands for the orientation of the molecule in the d^{rot}-dimensional space of the rotations. These manipulations finally yield in the limit $P \to \infty$ the exact path integral decomposition of the partition function (2.3):

$$Z(\beta) = \lim_{P\to\infty} \int \mathrm{d}\boldsymbol{r}_P \int \mathrm{d}\omega_P \int \mathrm{d}\boldsymbol{r}_{P-1} \int \mathrm{d}\omega_{P-1} \cdots \int \mathrm{d}\boldsymbol{r}_2 \int \mathrm{d}\omega_2 \int \mathrm{d}\boldsymbol{r}_1 \int \mathrm{d}\omega_1 \; \rho_{1P}(\beta/P) \times \rho_{PP-1}(\beta/P) \cdots \rho_{32}(\beta/P)\rho_{21}(\beta/P) \tag{2.10}$$

corresponding to the Hamiltonian (2.1), where $\rho_{tt+1}(\beta/P)$ denotes the high-temperature density matrix elements in the $(\boldsymbol{r}, \omega)$ representation.

The required Trotter limit $P \to \infty$ in (2.8) and thus also in (2.10) cannot be achieved in numerical path integration methods. However, the use of large Trotter numbers P allows one to neglect the $\mathcal{O}\{(\beta/P)^3\}$ terms on the right-hand side of (2.6) in practice. In the following, we assume sufficiently large P and refer the reader to [30, 49–51, 108, 152] for methods that extrapolate from finite P to the Trotter limit. This procedure is sometimes called Trotter scaling or Trotter extrapolation.

In order to evaluate the discretized path integral (2.10), we are left with the task of evaluating the elements of the Trotter approximant of the high-temperature density matrix

$$\rho_{tt+1}(\beta/P) = \langle \boldsymbol{r}_t\omega_t | \exp\left[-\beta\hat{V}/2P\right] \exp\left[-\beta(\hat{T}^{\mathrm{kin}} + \hat{T}^{\mathrm{rot}})/P\right] \exp\left[-\beta\hat{V}/2P\right] | \boldsymbol{r}_{t+1}\omega_{t+1}\rangle \tag{2.11}$$

that connects two succeeding Trotter slices t and $t+1$. As a result of the additive structure of the Hamiltonian (2.1) and the Trotter decomposition, the kernel $\rho_{tt+1}(\beta/P)$ can be factorized into three contributions. Because $\hat{V}$ is diagonal in coordinate space and because $\hat{T}^{\mathrm{kin}}$ and $\hat{T}^{\mathrm{rot}}$ commute in the rigid-rotor approximation, one obtains

$$\rho_{tt+1}(\beta/P) = \rho^{\mathrm{pot}}_{tt+1}(\beta/P)\rho^{\mathrm{tra}}_{tt+1}(\beta/P)\rho^{\mathrm{rot}}_{tt+1}(\beta/P) \tag{2.12}$$

with

$$\rho^{\mathrm{pot}}_{tt+1}(\beta/P) = \exp\left[-\frac{\beta}{2P}\left\{V(\boldsymbol{r}_t\omega_t) + V(\boldsymbol{r}_{t+1}\omega_{t+1})\right\}\right] \tag{2.13}$$

$$\rho^{\mathrm{tra}}_{tt+1}(\beta/P) = \langle \boldsymbol{r}_t | \exp\left[-\beta\hat{T}^{\mathrm{tra}}/P\right] | \boldsymbol{r}_{t+1}\rangle \tag{2.14}$$

$$\rho^{\mathrm{rot}}_{tt+1}(\beta/P) = \langle \omega_t | \exp\left[-\beta\hat{T}^{\mathrm{rot}}/P\right] | \omega_{t+1}\rangle. \tag{2.15}$$

The translational contribution $\rho^{\mathrm{tra}}_{tt+1}(\beta/P)$ can be calculated analytically for general dimension d by inserting an identity operator in the momentum representation, resulting in

$$\rho^{\mathrm{tra}}_{tt+1}(\beta/P) = \left(\frac{mP}{2\pi\hbar^2\beta}\right)^{d/2} \exp\left[-\frac{mP}{2\hbar^2\beta}(\boldsymbol{r}_t - \boldsymbol{r}_{t+1})^2\right] \tag{2.16}$$

with m the mass of the molecule. There is no such closed expression for $\rho^{\mathrm{rot}}_{tt+1}(\beta/P)$. This is what makes the simulation of rotational degrees of freedom a more difficult task than the simulation of translational degrees of freedom. The evaluation of the right-hand side of (2.15) is conveniently carried out separately for one-, two-, and three-dimensional rotation; see subsections 2.2, 2.3, and 2.4.

Given (2.1)–(2.16) and assuming that $\rho^{\mathrm{rot}}_{tt+1}(\beta/P)$ is known and strictly positive, it is possible to calculate thermal expectation values of the observables (2.4) depending exclusively on the spatial coordinates $\hat{O}(\hat{\boldsymbol{r}}\hat{\omega})$ via the sum

$$\langle \hat{O} \rangle = \frac{1}{P} \sum_{t=1}^{P} \langle O(\boldsymbol{r}_t\omega_t) \rangle \tag{2.17}$$

with $\prod_{t=1}^{P} \rho_{tt+1}(\beta/P)$ being the probability measure $\langle \cdots \rangle$ on the right-hand side of (2.17). The trace operation in (2.3) or (2.4) leads to periodic boundary conditions in imaginary time $|\boldsymbol{r}_{P+1}\omega_{P+1}\rangle \equiv |\boldsymbol{r}_1\omega_1\rangle$, which allows for the interpretation of the isomorphic classical system as a ring polymer or as a cyclic chain [21, 26, 27]. Once a positive probability measure and estimators for observables such as (2.17) are derived, it is possible to apply standard classical Monte Carlo, molecular dynamics, or Langevin dynamics techniques [1, 9, 10]. Such a simulation is then called path integral Monte Carlo or path integral molecular dynamics, because the variables $\{\boldsymbol{r}_1\omega_1, \ldots, \boldsymbol{r}_t\omega_t, \ldots, \boldsymbol{r}_P\omega_P\}$ define a path in a discretized 'imaginary time' t with a time step $\hbar\beta/P$. In [39, 40, 75, 137], a more general discussion of the path integral formulation of quantum statistical mechanics and path integrals can be found, whereas [21, 25, 35, 52, 135, 160] focus on reviewing simulation methods and their applications.

Not all of the techniques which have been developed for path integral simulations of translational degrees of freedom can be applied to the path integral treatment of rotational degrees of freedom in a straightforward manner. Important examples are pair density matrices [3, 21, 123], staging methods [68, 123, 142, 158, 160], and the use of virial estimators [38, 57, 119]. So far, staging and virial techniques have only been applied successfully to one-dimensional rotation [18]. Higher-order approximants for the high-temperature density matrix [33, 154] have only been applied to two-dimensional rotation [109], but their use is easily generalized to one-dimensional rotation. One of the most frequently used forms of higher-order approximants is the one proposed by Takahashi and Imada [79, 154], which is based on representing the partition function as

$$Z(\beta) = \lim_{P\to\infty} \mathrm{Tr}\left\{\exp\left[-\beta\hat{T}/P\right]\exp\left[-\beta(\hat{V}+\hat{V}^{\mathrm{corr}})/P\right]\right\}^{P} \tag{2.18}$$

with

$$\hat{V}^{\mathrm{corr}} = \frac{\beta^2}{24P^2}\left[\hat{V},\left[\hat{T},\hat{V}\right]\right] \tag{2.19}$$

and $\hat{T} = \hat{T}^{\mathrm{tra}} + \hat{T}^{\mathrm{rot}}$. Thus, the Trotter number P can be reduced at the expense of evaluating a temperature-dependent correction operator $\hat{V}^{\mathrm{corr}}$ to the potential.

How exchange effects are included into the simulation is an additional difference between the simulation of translational and rotational degrees of freedom. The best-known example for exchange effects influencing the rotational wave function is the hydrogen molecule that exists either as para-H_2, with even angular momentum, or as ortho-H_2, with odd angular momentum, depending on its total nuclear spin. The latter case is computationally difficult to treat, because the anti-symmetrized high-temperature density matrix has negative contributions, and the usual interpretation of $\prod_{t=1}^{P} \rho_{tt+1}(\beta/P)$ as a probability measure is no longer possible. An approximate way to deal with this problem is described in section 2.5.2. How to generate symmetrized high-temperature density matrices in general is dealt with in section 2.5.

We mention in passing that there is an alternative path integral approach for the simulation of quantum rotor impurities in classical environments [56, 107, 115]. In this approach the trace over an effective density matrix is taken in a reduced Hilbert space of the rotational degrees of freedom. This allows for the definition of a rotational free energy, which enters the relevant Boltzmann factor. Although the rotational degrees of freedom are practically treated in the quantum limit, we do not pursue this approach further here, because the method is tailored only for one single rotor in complex environments. The *rigorous* coupling of several rotors would require computer memory and computation time increasing exponentially with the number of directly coupled rotational degrees of freedom. The same arguments apply to a similar method proposed in references [12, 13], where the environment is allowed to be quantum mechanical;

see section 3.1.2. This method could nevertheless be extended to treat a few interacting rotors at the expense of invoking several assumptions and approximations [14].

2.2. One-dimensional rotation

In the case of one-dimensional rotation, the orientation of a molecule is defined by only one angle $0 \leqslant \varphi < 2\pi$ and the operator of the kinetic energy (2.2) has the form

$$\hat{T}_{\mathrm{rot}} = -B\,\frac{\partial^2}{\partial\varphi^2} \tag{2.20}$$

$$B = \frac{\hbar^2}{2\Theta} \tag{2.21}$$

with B the rotational constant and Θ the molecule's moment of inertia. The elements of the free-rotor density matrix in the representation of this coordinate φ can be calculated using (2.15) and inserting an identity operator composed of $d^{\mathrm{rot}} = 1$ free-rotor wave functions $|m_t\rangle$ with m_t the angular momentum at time slice t:

$$\rho^{\mathrm{rot}}_{tt+1}(\beta/P;\varphi_t,\varphi_{t+1}) = \left(\frac{P}{4\pi\beta B}\right)^{1/2}\sum_{n_t=-\infty}^{\infty}\exp\left[-\frac{P}{4\beta B}(\varphi_t-\varphi_{t+1}+2\pi n_t)^2\right]. \tag{2.22}$$

Use has been made of a Poisson summation formula [4]; see [15] for the first derivation in the framework of real-time path integrals and quantum dynamics. This leads to the following rotational part of the partition function:

$$Z^{\mathrm{rot}} = \lim_{P\to\infty}\left(\frac{P}{4\pi\beta B}\right)^{P/2}\prod_{t=1}^{P}\left[\sum_{n_t=-\infty}^{\infty}\int_0^{2\pi}\mathrm{d}\varphi_t\right]\exp\left[-\beta\sum_{t=1}^{P}\frac{P}{4\beta^2 B}(\varphi_t-\varphi_{t+1}+2\pi n_t)^2\right] \tag{2.23}$$

for one single free rotor. The set of variables $\{\varphi_1,\ldots,\varphi_P;n_1,\ldots,n_P\}$ is necessary to fully specify a path in imaginary time. This $\{n_t\}$-number representation is the most straightforward formulation of the partition function, allowing one to simulate one-dimensional rotational motion by path integral Monte Carlo methods. The earliest discussion of this formula for numerical path integral simulations known to the authors can be found in [2].

2.2.1. Winding number representation. Instead of carrying out the P-independent summations over $-\infty \leqslant n_t \leqslant \infty$ in (2.23) explicitly by Monte Carlo sampling, it is possible to transform to a less redundant set of variables. For invoking analogous ideas in connection with evaluating the propagator of one particle in a box, see [67]. It is convenient to define the following set of variables [18]:

$$\begin{aligned}
\tilde{\varphi}_1 &= \varphi_1\\
\tilde{\varphi}_2 &= \varphi_2 - 2\pi n_1\\
\tilde{\varphi}_3 &= \varphi_3 - 2\pi n_1 - 2\pi n_2\\
&\vdots\\
\tilde{\varphi}_t &= \varphi_t - 2\pi\sum_{t'=1}^{t-1} n_{t'}
\end{aligned} \tag{2.24}$$

where all of the $2\pi n_t$-terms cancel:

$$(\varphi_t-\varphi_{t+1}+2\pi n_t)^2 \longrightarrow (\tilde{\varphi}_t-\tilde{\varphi}_{t+1})^2 \qquad \text{for } t=1,\ldots,P-1 \tag{2.25}$$

but for the last contribution

$$(\varphi_P - \varphi_{P+1} + 2\pi n_P)^2 \longrightarrow \left(\tilde{\varphi}_P - \tilde{\varphi}_{P+1} + 2\pi \underbrace{\sum_{t=1}^{P} n_t}_{n}\right)^2 \tag{2.26}$$

where all P contributions sum up. This sum $n = \sum_{t=1}^{P} n_t$ denotes the winding number of the path. The winding number essentially counts how often a path leaves the basic angular interval $[0, 2\pi)$ taking into account the cancellation of positive and negative excursions since $-\infty \leqslant n_t \leqslant \infty$. Thus, the reduced set of variables $\{\tilde{\varphi}_1, \ldots, \tilde{\varphi}_P; n\}$ defines in this representation a path in imaginary time.

The peculiarity that one-dimensional rotational paths are only closed modulo 2π is a consequence of the paths being restricted to the $\mathcal{S}^1$ topology of the circle [137]. These manipulations yield the winding number representation [18, 87, 89]

$$Z^{\mathrm{rot}} = \lim_{P\to\infty}\left(\frac{P}{4\pi\beta B}\right)^{P/2} \sum_{n=-\infty}^{\infty} \int_0^{2\pi} \mathrm{d}\tilde{\varphi}_1 \prod_{t=2}^{P}\left[\int_{-\infty}^{\infty} \mathrm{d}\tilde{\varphi}_t\right] \times \exp\left[-\beta \sum_{t=1}^{P} \frac{P}{4\beta^2 B}(\tilde{\varphi}_t - \tilde{\varphi}_{t+1} + 2\pi n \delta_{t,P})^2\right] \tag{2.27}$$

of the rotational contribution to the total partition function of a free rotor. The total partition function is obtained by multiplication with the translational and potential contributions according to (2.12)–(2.15). It should be mentioned that the underlying Poisson summation leads in fact to a duality transformation [134] $\{m_t \rightarrow n_t\}$, which implies that the discrete variables n_t and thus the winding number n do *not* have the properties of angular momentum quantum numbers m_t. As a consequence, the classical limit is obtained in the quantum number representation (2.23) as usual by integration over m_t in addition to setting $P = 1$. In the winding number representation (2.27), however, the classical approximation is realized by taking into account only the $n = 0$ term of the full winding number spectrum (in addition to setting $P = 1$) [89]. Thus, the proper inclusion of the winding number leads in general to broader angular distributions such as the one obtained with the $n = 0$ restriction, which was explicitly demonstrated for model systems in [18].

The original angles φ_t are only defined on the interval $[0, 2\pi)$, whereas the transformed variables $\tilde{\varphi}_t$ are defined on $[-\infty, \infty]$ except for $\tilde{\varphi}_1$ which is still restricted to $[0, 2\pi)$. We refer the reader to section II B of [89] for a more detailed discussion of these aspects including the concept of homotopy classes as indexed by n and a more general mathematical justification of the transformation of (2.23) to the winding number representation (2.27). Exhaustive discussions of homotopy concepts in path integration and path integrals in multiply connected and curved spaces can be found in [75, 137].

Finally, a technical aspect connected to the Monte Carlo sampling with respect to the Boltzmann factor (2.27) needs to be mentioned. Since the winding number is a topological property of a given path, its value cannot be altered by small (local) displacements of a few angular degrees of freedom $\tilde{\varphi}_t$. To illustrate, one may imagine the path as a rope wound n times around an infinitely long stick. The rope's two ends are knotted together. Changing n to n' is only possible after cutting the rope, changing the number of loops around the stick, and re-knotting it again. Thus, the sampling of the sum over winding numbers $-\infty \leqslant n \leqslant \infty$ in the representation (2.27) calls for truly non-local Monte Carlo moves that include all P angles $(\tilde{\varphi}_1, \ldots, \tilde{\varphi}_P)$ as introduced in [89]. This is similar to the permutation moves that are necessary to sample bosonic exchange in translational path integration [21].

An illustration of representative paths that were generated by this algorithm are shown in figures 1 and 2 for high (200 K) and low temperatures (5 K) and for an isolated light (H_2) and heavy (N_2) homonuclear molecule. Each molecule is physisorbed on graphite and feels a static external potential (crystal field) due to the so-called herringbone ordering [98] of the surrounding molecules and the molecule–graphite interaction. In addition, the molecule is forced to rotate in the surface plane. This yields a distorted cosine potential with twofold rotational symmetry with minima at about 135° and 315° and correspondingly with maxima at about 45° and 225°. Since the particular model is not of interest here, we refer the interested reader to [89] for complete information.

The paths of the heavy molecule, N_2, at high temperatures—see figure 1(b)—are essentially straight lines, i.e., only weakly dependent on imaginary time. However, the angular density distribution function (not presented here, but see figure 8(b) in [89]) shows that a significant fraction of the paths are located on the *maxima* of the potential. Thus, the paths sweep like rigid sticks over the potential landscape, which is the signature of classical behaviour and thermally activated barrier crossing. In addition, the average angular spread (angular radius of gyration) of the paths amounts to less than 5° and the average winding number n is zero,

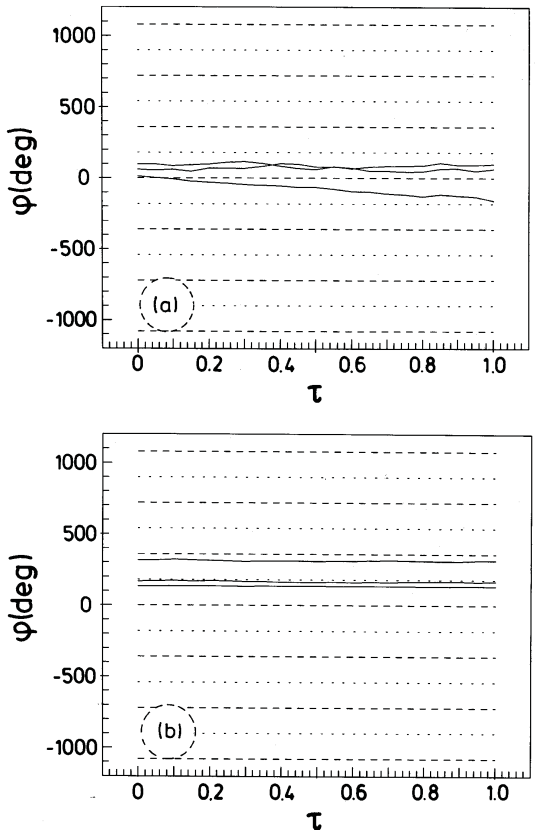

Figure 1. Three representative snapshots of angular paths $\varphi(\tau)$ from PIMC simulations of one rotating linear molecule ($d^{\mathrm{rot}} = 1$; external potential of twofold symmetry with minima at about 135° and 315° and maxima at about 45° and 225°) at 200 K as a function of the dimensionless imaginary time $\tau = t/P$ with $P = 20$. (a) H_2 (annealed simulation), (b) N_2 (no-spin simulation). Dotted and dashed lines mark the basic π- and 2π-periodicity, respectively. Adapted from [89].

which proves that quantum dispersion and thus zero-point motion is negligible. Thus, the path integral simulation generates quantitatively the expected picture of N_2 behaving like a classical rotor at high temperature.

This situation changes qualitatively for N_2 at 5 K; see figure 2(b). Here the paths stay in the potential wells 'most of the (imaginary) time' (as is also reflected by the angular density distribution; see figure 7(b) in [89]). However, inspection of the paths reveals that different parts of a given path are sitting in different potential wells. These barrier-crossing events have a kink-like shape as they occur typically on short (imaginary) timescales (and not gradually, involving the whole path), which is a signature of instanton-like tunnelling through the rotation barrier. Kinks and anti-kinks do not have to occur in pairs (as in translational tunnelling), because the winding number can account for such a mismatch. Furthermore, it can be seen that the paths do not have to be closed in the basic angular $[0, 2\pi)$ interval, but only modulo π, since the influence of the quantum exchange statistics of the bosonic nuclei on the rotational levels was included in this simulation (in the so-called quenched average; see section 2.5 and in particular section 2.5.1 for a discussion of various averaging concepts).

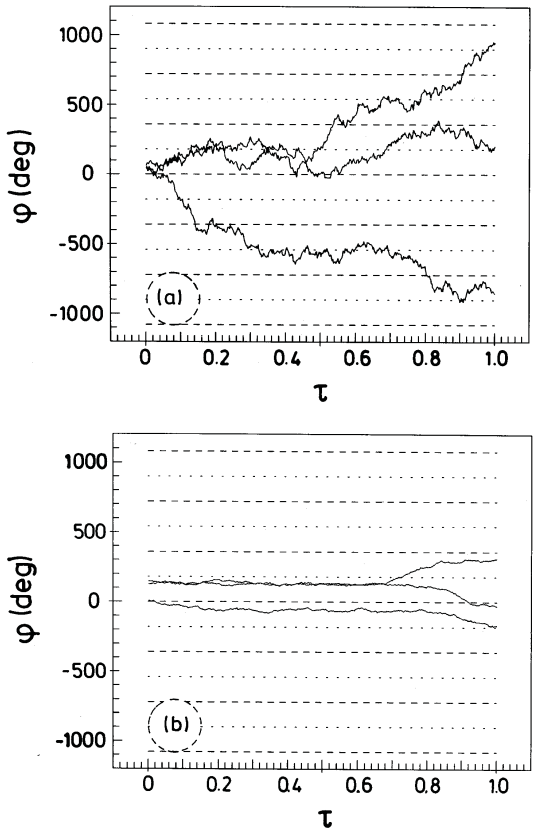

Figure 2. Three representative snapshots of angular paths $\varphi(\tau)$ from PIMC simulations of one rotating linear molecule ($d^{\mathrm{rot}} = 1$; external potential of twofold symmetry with minima at about 135° and 315° and maxima at about 45° and 225°) at 5 K as a function of the dimensionless imaginary time $\tau = t/P$ with $P = 540$. (a) H_2 (annealed simulation), (b) N_2 (quenched simulation with high-temperature composition). Dotted and dashed lines mark the basic π- and 2π-periodicity, respectively. Adapted from [89].

The high- and low-temperature behaviours of H_2 are in stark contrast to those of N_2. The modulation of the external potential is much weaker for H_2 than it is for N_2 [89]. The light molecule already shows at 200 K a spreading of individual paths over potential maxima; see figure 1(a). But in this case, the spreading results from a continuous deformation of entire paths taking place over the full imaginary time interval $\tau \in [0, 1)$. Thus, this situation corresponds more to a quantum dispersion broadening than to abrupt tunnelling events. At 200 K the quantum angular distribution function is essentially identical to the corresponding classical behaviour where thermal delocalization of the molecular axis occurs. Only a slight twofold density modulation remains as a signature of the weak external potential, which is free-rotor-like behaviour (see figure 8(a) in [89]).

At low temperatures, the H_2 paths are no longer very smooth and in particular they span several times over the basic $[0, \pi)$ interval without 'feeling' the underlying potential much. Therefore, they accumulate very large winding numbers; see figure 2(a). This leads to an enormous average angular spread of the paths of about 135°. Furthermore, the corresponding classical angular distribution at 5 K is tightly localized in the potential minima with basically no weight at the maxima, whereas the quantum system at 5 K shares the characteristics of the high-temperature situation at 200 K (see figure 7(a) in [89]). Thus, the reason for the free-rotor-like behaviour of H_2 at low temperatures is quantum delocalization by dispersion or zero-point effects. In conclusion, the proper treatment of the winding number is essential to simulate the correct quantum behaviour. This discussion also demonstrates how much can be learned about the mechanism of quantum processes by just analysing the geometric behaviour of the Trotter paths.

2.2.2. Decoupled winding number representation. The partition function in the winding number representation (2.27) can be simplified further such that it is better suited for numerical simulations [18]. This is achieved by making an additional variable transformation:

$$\bar{\varphi}_t = \tilde{\varphi}_t - 2\pi n\left(\frac{t-1}{P}\right) \qquad t = 1, \ldots, P \tag{2.28}$$

with $\bar{\varphi}_{P+1} = \bar{\varphi}_1 = \tilde{\varphi}_1$. This transformation was used in [87, 89] to generate trial paths for winding number changes in the Monte Carlo procedure. This change of variables yields the following expression:

$$Z^{\mathrm{rot}} = \lim_{P\to\infty}\left(\frac{P}{4\pi\beta B}\right)^{P/2} \sum_{n=-\infty}^{\infty} \int_0^{2\pi} \mathrm{d}\bar{\varphi}_1 \prod_{t=2}^{P}\left[\int_{-\infty}^{\infty} \mathrm{d}\bar{\varphi}_t\right] \times \exp\left[-\beta\left\{\sum_{t=1}^{P} \frac{P}{4\beta^2 B}(\bar{\varphi}_t - \bar{\varphi}_{t+1})^2 + \frac{(2\pi n)^2}{4\beta^2 B}\right\}\right] \tag{2.29}$$

for the rotational contribution to the partition function. It should be noted that the variable transformation has also to be applied in the evaluation of the potential

$$V(\boldsymbol{r}_t\tilde{\varphi}_t) \xrightarrow{(2.28)} V(\boldsymbol{r}_t\tilde{\varphi}_t + 2\pi n(t-1)/P) \tag{2.30}$$

in the separated potential energy propagator (2.13) according to the factorization (2.12). This means that the sum over all winding numbers cannot be taken before the angular integration and hence cannot be performed explicitly. But the winding number can be sampled as a random variable directly from a Gaussian distribution.

The net result of this transformation is a decoupling of the winding number from the angular degrees of freedom [18]. In particular, the angular term is now identical to the kinetic energy of standard translational path integrals and one can immediately see

that the second contribution gives paths with non-zero winding number a weight that falls off exponentially $\sim \exp\left[-\text{constant} \times n^2\right]$ with increasing winding number. Given a fixed temperature and a fixed molecular moment of inertia Θ, this means that only those paths that satisfy $(2\pi n)^2/2\lambda^2 \lesssim 1$ contribute significantly; here, $\lambda^2 = \hbar^2\beta/\Theta$ denotes an *angular* thermal wavelength in radians. Paths with large winding numbers in the sense $n/\lambda \gg 1$ do not contribute.

An advantage of the decoupled winding number representation (2.29) consists in it leaving one more freedom to construct efficient Monte Carlo sampling schemes separately for the winding number and in $\{\bar{\varphi}_t\}$-space as introduced in [18]. On the basis of the observation that paths with $n/\lambda \gg 1$ are not important, one can generate angular configurations by the Monte Carlo technique according to the $n = 0$ contribution

$$\sim \exp\left[-\beta \sum_{t=1}^{P} \frac{P}{4\beta^2 B}(\bar{\varphi}_t - \bar{\varphi}_{t+1})^2\right] \tag{2.31}$$

as for standard translational path integrals. Subsequently every configuration has to be reweighted by the explicit sum $\sum_{n=-n^{\max}}^{n^{\max}}$ that is taken up to a preset maximum winding number $n^{\max}$ such that $n^2/\beta B \gg 1$ is satisfied up to desired accuracy. Note that the potential has to be re-evaluated for every term in the sum according to (2.30), which makes this approach efficient for high temperatures where $n^{\max}$ is small. In the opposite limit, one could sample the winding number as a Gaussian random number instead of carrying out the n-summation explicitly. This sampling is similar to what is done in the winding number representation (2.27). This scheme leads effectively to fewer evaluations of the potential.

2.2.3. Alternative representations. In this section, alternative representations of the free-rotor kernel are introduced that are easy to implement and nevertheless exact in the limit $P \to \infty$.

The quadratic term in the $\{n_t\}$-number representation of the rotational partition function (2.23) is reminiscent of a small-ϕ expansion of $\cos\phi \sim (1 - \phi^2/2)$. In addition, $\cos(-\phi) = \cos(\phi)$ and the phase vanishes since $\cos(\phi + 2\pi n_t) = \cos\phi$, which suggests

$$(\varphi_t - \varphi_{t+1} + 2\pi n_t)^2 \approx 2[1 - \cos(\varphi_t - \varphi_{t+1})] \qquad \text{for } |\varphi_t - \varphi_{t+1} + 2\pi n_t| \to 0 \tag{2.32}$$

as an approximation to the action. This kind of inverse Villain transformation of the classical XY-spin model [70, 161] leads to the following representation of (2.23):

$$Z^{\text{rot}} = \lim_{P\to\infty}\left(\frac{P}{4\pi\beta B}\right)^{P/2} \prod_{t=1}^{P}\left[\int_0^{2\pi} \mathrm{d}\varphi_t\right] \exp\left[-\beta \sum_{t=1}^{P} \frac{P}{4\beta^2 B} 2\,[1 - \cos(\varphi_t - \varphi_{t+1})]\right]. \tag{2.33}$$

This was used in [63–65] to perform path integral simulations of $d = 2$ periodic arrays of ultrasmall Josephson junctions. In this system, the $d^{\text{rot}} = 1$ rotor contribution (2.23) represents the kinetic energy of the system due to the charging energy in the limit of no Josephson coupling.

For the particular application the angular degrees of freedom (having $\mathsf{U}(1)$ symmetry) were not treated as continuous variables but were discretized in order to speed up the algorithm. This leads to a $\mathsf{Z}(\mathsf{N})$ symmetry for a representation of $\varphi_t \in [0, 2\pi)$ using $\{\varphi_t^{(i)}\}$ with $i = 1, \ldots, \mathsf{N} \approx 5000$ points on the angular mesh. This kind of discretization does not lead to any significant systematic error in the calculation of observables as long the angular thermal wavelength at temperature PT is large compared to the discretization.

Given well-behaved potentials and finite P, the error in (2.33) vanishes with P^{-2} for constant temperature and moment of inertia. The deviation is not only due to the fact that kinetic and potential energy do not commute but also due to an approximate expression of the

free-rotor kernel. However, the representation is exact in the limit $P \to \infty$; see the analysis carried out in section II A in [70] and section III A in [65]. This is also physically intuitive, since the finer the discretization of the path the smaller $\langle|\varphi_t - \varphi_{t+1}|\rangle$ becomes and thus the better (2.32) is satisfied.

It is possible even to simplify (2.33) by using

$$Z^{\mathrm{rot}} = \lim_{P\to\infty}\left(\frac{P}{4\pi\beta B}\right)^{P/2}\prod_{t=1}^{P}\left[\int_0^{2\pi} \mathrm{d}\varphi_t\right]\exp\left[-\beta\sum_{t=1}^{P}\frac{P}{4\beta^2 B}(\varphi_t - \varphi_{t+1} + 2\pi i_t)^2\right] \qquad (2.34)$$

where $0 \leqslant \varphi_t < 2\pi$ and where i_t is chosen to be either -1, 0, or 1 such that it minimizes the action. The sum over i_t would correspond to an effective winding number. The i_t do not have to be sampled separately, but they are functions of the coordinates of the path. This property makes the simulations based on (2.33) or (2.34) easier to implement than methods which are based on a winding number representation.

It is unclear whether or not the simplified approach has been used in a study of orientational phase transitions in high-pressure solid molecular hydrogen [72]. The two-dimensional character of the H_2 rotor was reduced to a $d^{\mathrm{rot}} = 1$ problem by confining all molecules to rotate in symmetry planes of the crystal. The authors did not comment on how paths were closed and whether the winding number summation was performed, i.e., whether or not the term $2\pi i_t$ in (2.34) was included in the simulation. Omitting this term and allowing $-\infty \leqslant \varphi_t \leqslant \infty$ corresponds to neglecting the winding number altogether and yields too-narrow angular distribution functions; see section 2.2.1 or [18].

Using either representation, (2.33) or (2.34), care has to be taken with equilibration. Allowing only small displacements might have similar consequences to neglecting the winding number altogether. The algorithm is still exact in principle, but correlation times of the winding number run the risk of becoming huge. Therefore moves by of the order of $\pm 2\pi$ might be helpful to sample the winding number efficiently. Otherwise angular quantum fluctuations are suppressed, which leads to systematic errors in the observables. That is, estimates of phase transition temperatures in the low-temperature regime can be expected to be systematically too high. The magnitude of such an error seems difficult to assess without doing explicit calculations.

2.2.4. Approximate representations. Apart from the numerical evaluations of the exact path integral, it is also possible to apply the idea of quasi-classical approximations [37, 74, 103, 113, 138, 144, 145, 155, 163] to rotational degrees of freedom [47, 48, 88, 89, 97]. The central advantage of these methods is that they greatly reduce the computational effort of evaluating the full path integral. This is achieved by taking quantum fluctuations only approximately into account, thereby reducing the path integral to a standard Riemann integral. The latter can be evaluated by classical Monte Carlo or molecular dynamics simulation methods. One such approach is based on the Feynman–Hibbs effective potential that is particularly well suited for simulations, because it analytically approximates the path integral; see section 10-3 in [39]. The basic idea is to expand the full quantum paths in powers of the deviation from the path centroid, i.e., the average or mean path serves as the reference path. This is different from an expansion around the classical path as defined by the minimum of the action, which leads to WKB-like approximations. If truncated at second order in these fluctuations, the explicit kinetic energy contributions can be integrated out at the expense of introducing an additional term in the interaction potential. This term is temperature and mass dependent and vanishes in the classical limit. Given a certain 'bare' pair potential V for a N-rotor system with $d^{\mathrm{rot}} = 1$

rotational degrees of freedom per particle of the form

$$V = \sum_{i=1}^{N} V^{(1)}(\varphi_i) + \sum_{\langle i,j \rangle} V^{(2)}(\varphi_i, \varphi_j) \tag{2.35}$$

the resulting partition function reads [89]

$$Z_{\mathrm{FH}} = \left(\frac{1}{4\pi\beta B}\right)^{N/2} \prod_{i=1}^{N} \left[\int_0^{2\pi} \mathrm{d}\varphi_i\right] \exp\left[-\beta V_{\mathrm{FH}}(\beta)\right] \tag{2.36}$$

where

$$V_{\mathrm{FH}}(\beta) = V + \frac{\beta B}{12}\left\{\sum_{i=1}^{N} \frac{\partial^2}{\partial\varphi_i^2} V^{(1)}(\varphi_i) + 2\sum_{\langle i,j \rangle} \frac{\partial^2}{\partial\varphi_j^2} V^{(2)}(\varphi_i, \varphi_j)\right\} \tag{2.37}$$

denotes the Feynman–Hibbs effective potential. The explicit temperature dependence of $V_{\mathrm{FH}}(\beta)$ leads to additional terms in quantities obtained from temperature derivatives of the partition function, such as energy or heat capacity. The main advantage of the Feynman–Hibbs partition function (2.36)–(2.37) is that it can be evaluated by standard Monte Carlo methods at essentially the same cost as for a completely classical simulation [37, 138, 155]. The full path integral simulation is of course significantly more demanding. The price to be paid for this simplification is that such quasi-classical approximations are only useful for molecules with large moments of inertia and/or systems in the high-temperature limit. This is demonstrated in section 3.2.2 and in particular in figure 8 (see later).

2.3. Two-dimensional rotation

In the case of two-dimensional rotation the orientation of a molecule is defined by two angles $\Omega = (\vartheta, \varphi)$, and the operator of the kinetic energy (2.2) can be written as

$$\hat{T}_{\mathrm{rot}} = -B\left(\frac{\partial^2}{\partial\vartheta^2} + \cot\vartheta\,\frac{\partial}{\partial\vartheta} + \frac{1}{\sin^2\vartheta}\,\frac{\partial^2}{\partial\varphi^2}\right) \tag{2.38}$$

using the usual definition (2.21) of the rotational constant $B = \hbar^2/2\Theta$ with Θ the molecule's moment of inertia. The elements of the free-rotor density matrix in the coordinate representation Ω can be obtained as for one-dimensional rotation by inserting an identity operator in momentum representation into the right-hand side of (2.15). Using the addition theorem of spherical harmonics [166] leads to [94, 109]

$$\rho^{\mathrm{rot}}_{tt+1}(\beta/P; \Omega_t, \Omega_{t+1}) = \sum_{J=0}^{\infty} \frac{2J+1}{4\pi} P_J(\boldsymbol{e}_t \cdot \boldsymbol{e}_{t+1}) \exp\left[-\frac{\beta}{P} J(J+1) B\right] \tag{2.39}$$

where $\boldsymbol{e}_t = (\sin\vartheta_t \cos\varphi_t, \sin\vartheta_t \sin\varphi_t, \cos\vartheta_t)$ denotes the normalized vector indicating the molecule's orientation at Trotter slice t and $P_J(\cos\alpha_{t,t+1})$ stands for the Legendre polynomial of degree J.

Unfortunately, equation (2.39) cannot be further simplified analytically. It has been shown [94] that it is not convenient to treat J as a random variable in the way the winding number is used as a random variable in the case of one-dimensional rotation. This is due to the so-called sign problem [80, 141] that occurs as soon as an element of the high-temperature density matrix can become negative [34]. Here, the elements of $\rho^{\mathrm{rot}}(\beta/P)$ can become negative due to the Legendre polynomials and diverge where a sign change occurs; see in particular figure 1 in [94].

This sign problem is remedied if the summation over J in (2.39) is carried out explicitly [31, 109, 133, 148]. For finite temperatures, $\beta > 0$, the sum obviously converges. In

order to avoid long computation times in a simulation while evaluating $\rho^{\mathrm{rot}}_{tt+1}$, it is advantageous to tabulate $\rho^{\mathrm{rot}}(\beta/P)$ on a grid. Since β/P is fixed in a simulation, $\rho^{\mathrm{rot}}(\beta/P)$ depends only on the scalar product $-1 \leqslant \boldsymbol{e}_t \cdot \boldsymbol{e}_{t+1} \leqslant 1$. Note that the grid has to be made finer as β/P decreases. A severe sign problem occurs if the fermionic nature of rotors has to be taken into account. This situation is encountered for ortho-H_2 or para-D_2 molecules, where the summation in (2.39) is correspondingly restricted to odd J-values. A fixed-node treatment was introduced in [124] in order to cope with this problem in an approximate manner; see section 2.5.2 for a discussion.

It is also convenient to tabulate the estimator for the kinetic energy of the rotational degrees of freedom T^{est} if one wants to compute the rotational contribution to the internal energy $U(\beta)$. The primitive estimator can be obtained by exploiting the standard thermodynamic relation [3] $U(\beta) = -\partial \ln Z(\beta)/\partial\beta$, which gives [109]

$$\begin{aligned} T^{\mathrm{est}} &= \frac{1}{P}\sum_{t=1}^{P} T_t^{\mathrm{est}} \\ T_t^{\mathrm{est}} &= \frac{B}{4\pi\rho^{\mathrm{rot}}_{tt+1}} \sum_J (2J+1)J(J+1)P_J(\boldsymbol{e}_t \cdot \boldsymbol{e}_{t+1}) \exp\left[-\frac{\beta}{P}J(J+1)B\right]. \end{aligned} \tag{2.40}$$

Staging methods [123, 142, 158], improving the sampling efficiency for large Trotter numbers P, have not yet been derived for two-dimensional rotation. Thus, it is particularly rewarding to use higher-order approximants for the density matrix such as the one introduced in (2.18). This allows one to use smaller P-values while preserving the accuracy of the path integration. If only rotational degrees of freedom are present, the correction potential (2.19) reads [109]

$$\hat{V}^{\mathrm{corr}} = \frac{\beta^2 B}{12P^2}\left\{(\nabla\hat{V})^2 - \left[\boldsymbol{e}\cdot(\boldsymbol{\nabla}\hat{V})\right]^2\right\} \tag{2.41}$$

with $\nabla = (\partial/\partial e_1, \partial/\partial e_2, \partial/\partial e_3)$. The internal energy $U(\beta)$ can be obtained as usual in the Takahashi–Imada form [79, 154] as

$$U(\beta) = \frac{1}{P}\sum_{t=1}^{P}\left\langle T_t^{\mathrm{est}} + V_t + 3V_t^{\mathrm{corr}}\right\rangle \tag{2.42}$$

with $V_t = V(\Omega_t)$ and $V_t^{\mathrm{corr}} = V^{\mathrm{corr}}(\Omega_t)$. Thermal averages of observables $\hat{O}$ that are diagonal in the coordinate representation are obtained as [109]

$$\langle\hat{O}\rangle = \frac{1}{P}\sum_{t=1}^{P}\left\langle O_t + \frac{\beta^2 B}{6P^2}(\nabla V_t - \boldsymbol{e}_t\cdot\boldsymbol{\nabla}V_t)(\nabla O_t - \boldsymbol{e}_t\cdot\boldsymbol{\nabla}O_t)\right\rangle \tag{2.43}$$

with $O_t = O(\Omega_t)$.

2.4. Three-dimensional rotation

In the case of three-dimensional rotation the orientation of a molecule is defined by its three Euler angles $\omega = (\varphi, \vartheta, \chi)$ that relate the molecule-fixed frame to the laboratory-fixed frame. Depending on the value of its three principal moments of inertia ($\Theta_{\mathrm{aa}}, \Theta_{\mathrm{bb}}, \Theta_{\mathrm{cc}}$), a (non-linear) molecule is called asymmetric top if $\Theta_{\mathrm{aa}} < \Theta_{\mathrm{bb}} < \Theta_{\mathrm{cc}}$, spherical top if $\Theta_{\mathrm{aa}} = \Theta_{\mathrm{bb}} = \Theta_{\mathrm{cc}}$, oblate symmetric top for $\Theta_{\mathrm{aa}} = \Theta_{\mathrm{bb}} < \Theta_{\mathrm{cc}}$, or prolate symmetric top in the case where $\Theta_{\mathrm{aa}} < \Theta_{\mathrm{bb}} = \Theta_{\mathrm{cc}}$. Associated with the three moments of inertia are rotational constants $B_{\mathrm{a}} = \hbar^2/2\Theta_{\mathrm{aa}}$, etc. For more details on three-dimensional rotation; see chapter 6.3 in [166] and references therein. In the following, we will content ourselves with providing the formulae necessary to calculate the free-rotor density matrix.

First, the general case, namely the asymmetric top, will be considered; see section I.4 in [58] for a pictorial discussion of this motion. As in the case of one- and two-dimensional rotation, an exact expression for the free-rotor kernel can be obtained by inserting an identity operator in momentum representation into the right-hand side of (2.15). This yields [110]

$$\rho^{\mathrm{rot}}_{tt+1}(\beta/P;\omega_t,\omega_{t+1}) = \sum_{J=0}^{\infty}\frac{2J+1}{8\pi^2}\sum_{M=-J}^{J}\sum_{\tilde{K}=-J}^{J} d^J_{MM}(\tilde{\vartheta}_{tt+1})\cos[M(\tilde{\varphi}_{tt+1}+\tilde{\chi}_{tt+1})] \times \left|A^{(JM)}_{\tilde{K}M}\right|^2 \exp\left[-\beta E^{(JM)}_{\tilde{K}}/P\right] \tag{2.44}$$

with $\tilde{\omega}_{tt+1}$ denoting the Euler angles ω_{t+1} expressed in the molecule-fixed frame of ω_t, $d^J_{MM}(\vartheta)$ the Wigner functions, and $E^{(JM)}_{\tilde{K}}$ the eigenenergies of the asymmetric top [166]. The coefficients $A^{(JM)}_{\tilde{K}M}$ can be obtained by solving the secular equation

$$\hat{T}_{\mathrm{rot}}\sum_K A^{(JM)}_{\tilde{K}K}\Psi_{JMK} = E^{(JM)}_{\tilde{K}}\sum_K A^{(JM)}_{\tilde{K}K}\Psi_{JMK} \tag{2.45}$$

where Ψ_{JMK} denote the eigenstates of a symmetric top for which at least two moments of inertia are identical. To be specific, the non-zero $\hat{T}^{\mathrm{rot}}$-matrix elements in the prolate symmetric top basis set are given by

$$\langle JKM|\hat{T}_{\mathrm{rot}}|JKM\rangle = \tfrac{1}{2}(B_{\mathrm{b}}+B_{\mathrm{c}})[J(J+1)-K^2]+B_{\mathrm{a}}K^2 \tag{2.46}$$

$$\langle JKM|\hat{T}_{\mathrm{rot}}JK\pm 2\rangle = \tfrac{1}{4}(B_{\mathrm{b}}-B_{\mathrm{c}})[J(J+1)-K(K\pm 1)]^{1/2} \times [J(J+1)-(K\pm 1)(K\pm 2)]^{1/2}. \tag{2.47}$$

As for the two-dimensional rotation, it is recommended that the free-rotor high-temperature density matrix is tabulated in a PIMC simulation so that the expression (2.44) does not have to be computed at each Monte Carlo trial move.

An alternative way to evaluate $\rho^{\mathrm{rot}}_{tt+1}(\beta/P;\omega_t,\omega_{t+1})$ and thus the full path integral for general rotating rigid bodies is to compute the high-temperature (or 'short-time') density matrix in the semi-classical approximation. In this approximation, the orientation density matrix for a rigid body is given by [136]

$$\rho^{\mathrm{rot}}_{tt+1}(\beta/P;\omega_t,\omega_{t+1}) = C\,D^{1/2}(\beta/P;\omega_t,\omega_{t+1})\exp\left[-\frac{1}{\hbar}S_{\mathrm{cl}}(\beta/P;\omega_t,\omega_{t+1})\right] \tag{2.48}$$

where C is a constant, $D(\beta/P;\omega_t,\omega_{t+1})$ is the Van Vleck determinant associated with the rotation from ω_t to ω_{t+1} in a time period of $\beta\hbar/P$, and $S_{\mathrm{cl}}(\beta/P;\omega_t,\omega_{t+1})$ is the action along the least-action classical path between the end-points in the given time interval. The determinant D includes rigorously quadratic fluctuations around the classical path; see [75, 137] for thorough discussions of the semi-classical approximation in the framework of path integrals. The exact evaluation of this fluctuation determinant for a general asymmetric top molecule is a non-trivial task of classical mechanics, because there is no special internal axis of rotation; see section I.4 in [58] for a discussion. However, for short time intervals it is consistent to evaluate the action corresponding to the rotation connecting ω_t and ω_{t+1} around a *fixed axis* at constant angular velocity [77, 78]. The resulting Van Vleck determinant in this so-called fixed-axis approximation is given by [77, 78]

$$D(\beta/P;\omega_t,\omega_{t+1}) \approx D_{\mathrm{FA}}(\beta/P;\omega_t,\omega_{t+1}) = \frac{\Theta_{aa}\Theta_{bb}\Theta_{cc}}{(\beta\hbar/P)^3}\left(\frac{\Gamma_{t,t+1}}{2\sin(\Gamma_{t,t+1}/2)}\right)^2 \tag{2.49}$$

where $\Gamma_{t,t+1}$ is the associated arc length of the rotation. This expression can be substituted in (2.48) together with the associated action $S_{\mathrm{FA}}(\beta/P;\omega_t,\omega_{t+1})$. The overall error of the fixed-axis semi-classical approximation can be shown to be $\mathcal{O}\{(\beta/P)^2\}$. Thus, the full path integral

according to the decomposition outlined in section 2.1 is numerically exact for sufficiently fine Trotter discretizations of the paths. This approach was used in order to investigate light and heavy liquid water at room temperature using both PIMC [77, 78] and PIMD [32] sampling techniques; see section 3.3.3 for a presentation of this study.

2.5. Coupling to nuclear spins

The spins of the nuclei involved in the rotation of a molecule implicitly constrain the symmetry of the rotational state even in the absence of a direct coupling between nuclear spins and rotational degrees of freedom [102, 156]. The absence of this direct coupling will be assumed in the following presentation. The symmetry conservation of the rotational wave function is a direct consequence of the symmetry requirement concerning the *total* wave function under exchange of identical particles, i.e., anti-symmetry for fermions and symmetry for bosons. It can be argued that in the limit of a weak coupling between electronic, vibrational, rotational, translational, and nuclear degrees of freedom, it is the combined rotational–nuclear wave function that determines the overall symmetry of an isolated molecule in its electronic ground state [102, 128]. While for heteronuclear polyatomic molecules the combined rotational–nuclear partition function $Z^{\mathrm{nuc-rot}} = Z^{\mathrm{nuc}} \otimes Z^{\mathrm{rot}}$ simply factors as $Z^{\mathrm{nuc}} Z^{\mathrm{rot}}$, the partition function of homonuclear polyatomic molecules instead decomposes as [89, 102]

$$Z^{\mathrm{nuc-rot}} = \sum_{\mu} g_{\mu} Z^{\mathrm{rot}}_{\mu} \tag{2.50}$$

where μ labels the representation, e.g., even (g) and odd (u) parity for diatomic homonuclear molecules. Z^{rot}_{μ} denotes the rotational partition function in representation μ and g_{μ} is the associated nuclear spin multiplicity (stemming from the nuclear partition function together with the fact that nuclear excitations can be neglected at the relevant temperatures). Thus, the summation over rotational levels that leads to Z^{rot}_{μ} has to be performed separately under the constraint of a fixed symmetry. These subtleties vanish of course in the classical limit, where the summation over rotational levels is replaced by an integration and only the multiplicative 'symmetry number' remains.

Once the effects due to exchange of identical nuclei are realized, several possible ways of performing thermodynamic averages are seen to exist. There are two types of experimental set-up for investigating homonuclear diatomic molecules; see [139] for a lucid presentation for the case of hydrogen molecules. First of all, one can prepare a sample with an arbitrary composition of the different μ-species (such as ortho- and para-species in the case of homonuclear diatomics). Since only $\mu \leftrightarrow \mu$ and not $\mu \leftrightarrow \mu'$ transitions are phonon induced [128], the thermal spin conversion is a slow process, and an assembly of molecules with an athermal non-equilibrium composition is approximately stable on typical experimental timescales. In such a sample, only the rotational degrees of freedom are changing fast enough to equilibrate. Thus, the different μ-species can be considered to be different species of the same chemical molecule. Consequently, a sample prepared and completely equilibrated at a given inverse temperature $\beta^{\star}$ can be cooled down or heated up to another temperature, β, while keeping the μ-composition constant. This leads to a thermal population of the rotational levels at temperature β, whereas the nuclei preserve the composition according to the thermal mixture at temperature $\beta^{\star}$. Another experimental realization would be to enrich the sample arbitrarily with some μ-species, thus producing any desired composition [139]. In statistical mechanics these schemes correspond to quenched averages where only a subset of all degrees of freedom (here the rotations but not the nuclear spins) is assumed to be in thermal equilibrium at some temperature, whereas the other degrees of freedom are frozen.

An alternative way to conduct experiments is to add a suitable catalyst [60] that accelerates the nuclear spin interconversion $\mu \leftrightarrow \mu'$ so that molecules that are in thermal equilibrium with both the nuclear spins and the rotations can be studied. This corresponds to the concept of an annealed average, where all degrees of freedom equilibrate at a given temperature. As an additional theoretical tool, a no-spin average can also be defined, where nuclear exchange and thus the symmetry restriction is neglected. It serves as a tool for separating the quantum effects due to indistinguishability of the nuclei from the dispersion effects due to the discrete spacing of the rotational levels. The three different quantum statistical averages were introduced and discussed for rotational motion in [56, 87, 89].

Finally, we note again that the coupling of the rotational motion to the nuclear spin state becomes irrelevant in the limit of high temperatures and/or large moments of inertia; see [73, 101] for explicit demonstrations based on calculating restricted partition functions.

2.5.1. Diatomic molecules. The simplest and best-known examples are the homonuclear diatomics H_2 and D_2, where the rotational state only depends on the symmetry of the nuclear wave function and the nuclear spin I; see [102, 156] for a discussion. Fermionic diatomic H_2 with $I = 1/2$ has three symmetric combinations and one anti-symmetric combination of the two nuclear spin functions. Since the overall symmetry with respect to exchange of the two nuclei must be anti-symmetric, the symmetric spin combinations allow only for odd rotational quantum numbers $Z^{\rm rot}_{\rm odd}$; this species is called ortho-H_2, and $g_{\rm odd} = 3$. Conversely, the anti-symmetric spin function forces the rotational levels to be even and couples to $Z^{\rm rot}_{\rm even}$ (para-H_2, $g_{\rm even} = 1$). For D_2 with $I = 1$, the result is that the three anti-symmetric (six symmetric) nuclear spin functions couple with only odd (even) rotational levels, leading to the para-D_2 (ortho-D_2) species. In the case of the heteronuclear diatomic molecule HD with its two distinguishable nuclei, all rotational levels are populated according to their Boltzmann weight, which is formally equivalent to $I = 0$ with equal weights, g_μ, of the even and odd rotational partition functions.

The concept of the three different quantum statistical averaging procedures is now explicitly formulated for one homonuclear diatomic molecule confined to rotate in a plane, i.e. $d^{\rm rot} = 1$. This is achieved by applying a generalized Poisson summation separately to the even and odd rotational levels [87, 89]; see [2] for an early discussion of some aspects connected to this procedure. The partition function for annealed averaging reads

$$Z^{\rm rot}_{\rm annealed} = \lim_{P\to\infty}\left(\frac{P}{4\pi\beta B}\right)^{P/2}\sum_{n=-\infty}^{\infty}\int_0^{\pi}{\rm d}\tilde{\varphi}_1\prod_{t=2}^{P}\left[\int_{-\infty}^{\infty}{\rm d}\tilde{\varphi}_t\right] \times \exp\left[-\beta\sum_{t=1}^{P}\frac{P}{4\beta^2 B}(\tilde{\varphi}_t - \tilde{\varphi}_{t+1} + \pi n\delta_{t,P})^2 + \ln(|g_g + g_u\exp[{\rm i}\pi n]|) + {\rm i}\sigma\right] \tag{2.51}$$

where the phase σ is a result of the generalized Poisson transformation and depends on the nuclear spin: $\sigma = \pi n$ for fermionic nuclei (e.g., H_2 with $I = 1/2$) and $\sigma = 0$ for bosonic nuclei (e.g., D_2 with $I = 1$). Quenched averages are obtained by weighting the free energies of the different symmetry classes or representations $\{\mu\}$ separately as

$$F^{\rm rot}_{\rm quenched}(\beta) = -\frac{1}{\beta}\sum_{\mu} q_\mu \ln(g_\mu Z^{\rm rot}_\mu(\beta)) \tag{2.52}$$

where the quench coefficients q_μ that weight the contributions of the various μ-species in the sample have only to satisfy the restriction $\sum_\mu q_\mu = 1$. Finally, the no-spin case (which is exact only for heteronuclear molecules) is obtained using the partition function (2.27). Again, the

corresponding total partition functions are obtained after multiplication with the translational and potential contributions according to (2.12)–(2.15).

Comparison of the partition function which includes the exchange statistics (2.51) with the one that neglects this constraint (2.27) reveals an interesting topological aspect of rotational motion in one dimension. The basic interval for the rotation is no longer $[0, 2\pi)$ as in the unconstrained case but is now $[0, \pi)$, since the paths are closed modulo π instead of modulo 2π. Thus, the paths are now defined on a 'circle with π-periodicity'. In addition, the last term $i\sigma$ in the Boltzmann factor of (2.51) assigns for fermions like H_2 a *negative weight* to paths with odd winding numbers. Thus, one has to separate the sign of the integrand and to determine its average separately [80, 89, 141], which is currently intractable for many-fermion systems due to statistics problems. Finally, it should be pointed out that the last two terms in the exponential of (2.51) can be considered as the real and imaginary parts of a complex chemical potential (in the sense of grand canonical formulation), similarly to the case of the translational partition function of fermions [26, 27]. The real part is only a trivial constant for a given winding number, whereas the imaginary part carries the non-trivial sign in the fermionic case. Thus, the (in)famous fermionic sign problem has to be faced for pure rotations too. See [22] for an in-depth discussion of the state-of-the-art sampling concerning translational path integrals with fermionic exchange.

The type of the averaging procedure can have profound effects on thermodynamic properties of the system. This is demonstrated again with a single heavy (N_2 with bosonic exchange) and a light (H_2 with fermionic exchange) $d^{\mathrm{rot}} = 1$ rotor in an external potential with twofold symmetry [87, 89]. In figures 3 and 4, the three path integral quantum statistical averages are also compared to the numerically exact variational solution of the one-dimensional Schrödinger equation [115] with subsequent explicit restricted summation over the energy levels. We note in passing that the excellent agreement demonstrates the validity of the

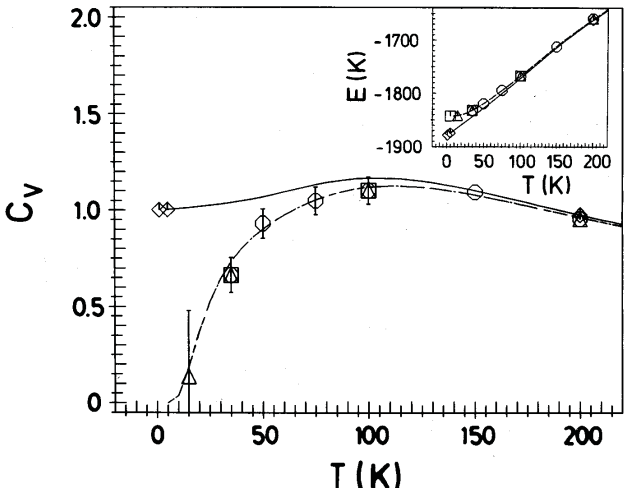

Figure 3. The heat capacity C_v and energy E (inset) from PIMC simulations of a single rotating N_2 molecule with $d^{\mathrm{rot}} = 1$ as a function of temperature in an external potential of twofold symmetry. The curves are numerically exact variational results (solid: classical average; dotted: no-spin; dashed: quenched with high-temperature composition; dashed–dotted: annealed) and the symbols are PIMC results (diamonds: classical average; triangles: no-spin; squares: quenched with high-temperature composition; circles: annealed). For clarity, only representative error bars are shown for C_v. Adapted from [89].

simulation technique.

For N_2 the three quantum statistical averages for the total energy and heat capacity collapse onto just one curve down to the lowest temperature investigated and approach the classical curve with increasing temperature; see figure 3. The situation is totally different for H_2, where the three quantum statistical averages already deviate below about 100 K from each other and show a distinctly different behaviour in the low-temperature regime; see figure 4. In the high-temperature limit all curves approach each other and nuclear spin coupling is observed to not play a rôle. See [73] for an early treatment based on the Euler–MacLaurin expansion technique for high temperatures and/or large moments of inertia. These differences are discussed and rationalized in [89]. Here we mention only that the differences between the no-spin and the classical curves are entirely due to the discrete level spacing whereas the difference between the three quantum averages is due to coupling to the nuclear spins and thus to exchange symmetry. In conclusion, this confirms the expectation that the coupling of the rotations to nuclear spin is only important for molecules with large rotational constants at low temperatures.

2.5.2. The restricted path integral method. As mentioned above, there are various situations where wave functions have to be symmetrized or anti-symmetrized in order to take into consideration nuclear spins and the fermionic or bosonic nature of particles. Instead of (anti-) symmetrizing the wave functions or high-temperature matrices themselves, it is also possible to restrict paths or to consider new paths. To restrict a path usually means to forbid the rotors to cross certain nodes, which is why we will use 'restricted path integral method' and 'fixed-node approximation' as synonyms.

Let us first consider even angular momentum and one-dimensional rotation. Instead of symmetrizing the free-rotor kernel, one could take the non-symmetrized kernel and allow the

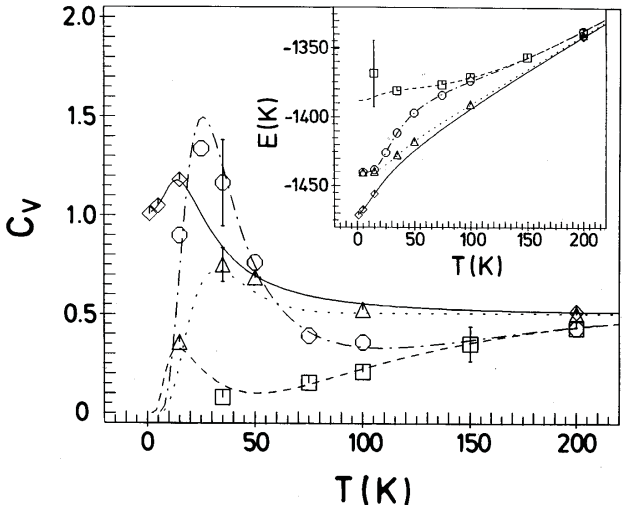

Figure 4. The heat capacity C_v and energy E (inset) from PIMC simulations of a single rotating H_2 molecule with $d^{\mathrm{rot}} = 1$ as a function of temperature in an external potential of twofold symmetry. The curves are numerically exact variational results (solid: classical average; dotted: no-spin; dashed: quenched with high-temperature composition; dashed–dotted: annealed) and the symbols are PIMC results (diamonds: classical average; triangles: no-spin; squares: quenched with high-temperature composition; circles: annealed). For clarity, only representative error bars are shown for C_v. Adapted from [89].

path to close after integer multiples of π. Hence, the periodic boundary condition in imaginary time reads $\varphi(\tau) = \varphi(\tau + \beta) + n\pi$. This is nothing but the well-known concept of the winding number; see section 2.2.1. The difference between the symmetrized and non-symmetrized kernel is that, in the latter case, paths are closed after 2π. In the case of two-dimensional rotation, a symmetrized path would be allowed to close not only at the initial point (ϑ, φ) but also at $(\pi - \vartheta, \pi + \varphi)$. This method is exact and corresponds to the way exchange is realized in the context of translational degrees of freedom and bosonic species [21].

The procedure is a little more complex for anti-symmetric rotational states. The anti-symmetrized kernel has negative contributions and consequently there are nodal surfaces where the density matrix vanishes. A nodal surface can never be crossed using infinitely small imaginary time steps. It has been shown that restricting the path integral to be only over node-avoiding walks is equivalent to demanding that the density matrix vanishes on the surface [22]. This means for one- and two-dimensional rotation that restricted paths are limited to be on a semi-circle or on a half-sphere only. This restriction only applies to moves in imaginary time. However, the orientation of the nodal surface can change from one Monte Carlo step to another [124]. In practice, the following procedure seems convenient. A random rotation is applied to the orientation of the nodal surface as well as to the orientation of every bead in the chain representing the rotor's trajectory in imaginary time. The acceptance criterion for such a trial move would then be a classical Metropolis algorithm.

It is easy to see that this algorithm leads to the right free-particle behaviour for one-dimensional rotation. For a given orientation of the nodal surface, e.g., $\alpha = \pi/2$, the Hilbert space spanned by the fixed-node approximation consists of wave functions that satisfy the boundary condition, namely $\psi_n \propto \sin[(2n + 1)\varphi]$. These wave functions can be generated by combinations of wave functions $\exp(\pm i(2n + 1)\varphi]$, which span the full space of $d^{\mathrm{rot}} = 1$ anti-symmetric wave functions. Moving the orientation of the nodal surface makes the Hilbert space of the odd angular states complete and reinstalls rotational invariance. Hence, the Hilbert space of one-dimensional rotation is spanned properly. The idea of fixed nodes has been applied to the PIMC simulation of solid ortho-H_2 [124]; see section 3.3.1 for a discussion of this application.

The fixed-node approximation is supposed to be exact if the nodes are known exactly [20, 22]. However, it has been argued that the free-rotor nodes will not always be exact in many-particle systems, because the potential field from other rotors may break the spherical symmetry [124]. Unfortunately, we are not aware of any published systematic study that focuses on the deviation between an exact and a fixed-node treatment of rotors with odd angular momentum.

If a fixed-node approximation is used, one should not rely on the primitive propagator and impose the constraints by brute force. In the case of fixed walls, it has been shown that the convergence behaviour is as slow as $P^{-1/2}$ [111]. Propagators based on so-called periodic images, such as the ones introduced in references [3] and [17], show much faster convergence to the quantum limit, e.g., using two images makes the corrections to the free-particle propagator vanish as fast as P^{-8} [111].

The fixed-node approximation cannot be applied in the case of an annealed average, because there is no longer symmetry in the wave function between the negative and the positive contribution. Finally, we point out that the sign problem is only present if $g_u > g_g$. A further discussion of the fixed-node approximation for rotors can be found in [20] and more recently in chapter 16.6 of [22].

2.5.3. Polyatomic molecules. Other well-studied examples where the symmetry restriction of the rotational partition function is crucial are rotating methyl groups ($-CH_3$) in solids [128].

These groups possess an *intrinsic* threefold rotation axis due to the nuclear exchange symmetry. Another example is CH_4, for which rotational spectra and thermodynamic properties depend on the symmetry of the rotational wave function [55, 165]; see section 3.3.2 for a discussion of solid methane.

In these more complicated situations, it is advantageous to use group theory to find, classify, and project out the relevant symmetry classes. It is generally possible to generate states belonging to representation μ with the help of projection operators [62, 156]

$$\hat{P}_\mu = \frac{d_\mu}{g} \sum_R \chi_R^{(\mu)} \hat{D}(R) \tag{2.53}$$

where the sum goes over all symmetry operations R. In (2.53), $\hat{D}(R)$ generates the symmetry operation, $\chi_R^{(\mu)}$ denotes the character of R in the representation μ, g is the order of the group, and d_μ is the dimension of the representation μ. Since the potential energy is invariant under a symmetry operation, it is convenient to exploit the projection-operator properties of P_μ and to symmetrize the elements of the high-temperature density matrix rather than to symmetrize the states themselves [110]:

$$\rho_\mu^{\mathrm{rot}}(\beta/P; \omega_t, \omega_{t+1}) = \frac{d_\mu}{g} \sum_R \chi_R^{(\mu)*} \rho^{\mathrm{rot}}(\beta/P; 0, \tilde{\omega}_{tt+1}(R)) \tag{2.54}$$

with $|\tilde{\omega}(R)\rangle = \hat{D}^+(\omega)\hat{D}(R)|\omega\rangle$. In the case of one-dimensional and two-dimensional rotation, the symmetrization procedure (2.54) just consists of symmetrizing or anti-symmetrizing ρ^{rot} with respect to a rotation by an angle π. Alternatively, identity operators in the subspace of even angular momentum and odd angular momentum may be inserted into (2.15) in order to symmetrize or anti-symmetrize ρ^{rot}, respectively.

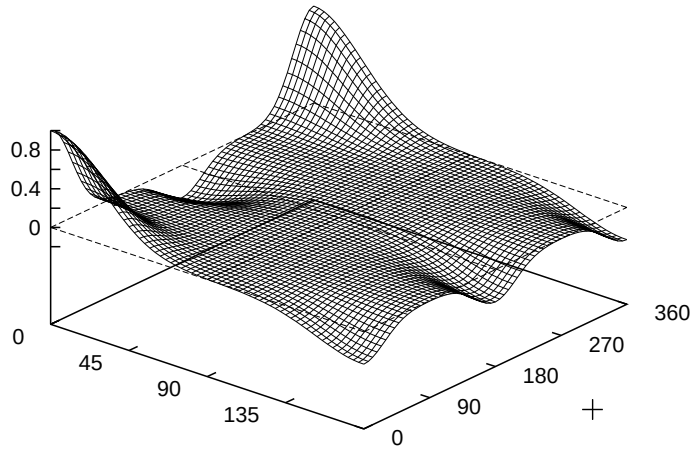

Figure 5. The free-rotor density matrix $\rho(\beta/P; 0, 0, \vartheta, \varphi + \chi)$ for CH_4 at $(\beta/P)^{-1} = 64\ k_B$K in the T representation which is one of the four symmetry classes of the tetrahedral group. Adapted from [110].

An example for a symmetrized kernel is shown in figure 5, namely the free-particle propagator in imaginary time for an individual CH_4 molecule in the T representation. The T representation is one of the four symmetry classes of the tetrahedral group, but it is not the identity representation. Note the negative contributions of the propagator in this representation. See figure 1 in [110] for the no-spin kernel and the kernel in the identity representation that are both strictly positive.

As in the case of diatomics, each representation for the rotation of polyatomic molecules has its own contribution to the total partition function. In the case of annealed averages, each representation enters the density matrix $\hat{\rho}^{\mathrm{rot}}_{\mathrm{annealed}}$ with an effective weight g_μ:

$$\hat{\rho}^{\mathrm{nuc-rot}}_{\mathrm{annealed}}(\beta) = \sum_\mu g_\mu \hat{\rho}^{\mathrm{rot}}_\mu(\beta). \tag{2.55}$$

However, $\hat{\rho}^{\mathrm{rot}}_{\mathrm{annealed}}(\beta)$ cannot be expressed as the product of P factors $\hat{\rho}^{\mathrm{rot}}_{\mathrm{annealed}}(\beta/P)$ but is instead given by

$$\hat{\rho}^{\mathrm{nuc-rot}}_{\mathrm{annealed}}(\beta) = \prod_{t=1}^{P} \left[\sum_{\mu_t} g_{\mu_t}^{1/P} \hat{\rho}^{\mathrm{rot}}_{\mu_t}(\beta/P) \right]. \tag{2.56}$$

Depending on the factors g_μ, the sign problem may be present or absent. A large degeneracy factor of the nuclear spins in the identity representation favours the absence of the sign problem.

In the no-spin case the path integral probability measure is always positive as it is for the identity representation. Other representations always have negative contributions in the associated path integral probability measure [110]. In this case the sign problem might be partially remedied by employing a fixed-node approximation; see section 2.5.2.

3. Selected applications

The investigation of quantum mechanical rotational motion of molecules in condensed phases is a topic of long-standing interest which dates back to the early days of quantum mechanics [120, 143]. One of the reasons for this is that quantum fluctuations of rotational degrees of freedom often lead to a considerable renormalization of classical behaviour. As an example, one can consider the temperature-driven orientational disordering transition in solid N_2. The transition temperature T_c for a simple classical model ($B = 0$) of solid N_2 is $T_c = 42.5$ K, while the quantum model (using $B_{N_2} = 2.8\ k_B$K) with the same potential energy surface shows a similar transition from an orientationally ordered to a plastic crystal at $T_c = 38\ (\pm 0.5)$ K [125]. The experimental transition temperature is found to be at $T_c = 35$ K. A more striking correction is found in the sublimation energy E_S, which experimentally is $E_S^{\mathrm{exp}} = 833\ k_B$K, while classical and quantum mechanical simulations yield approximately $E_S^{\mathrm{cl}} = 1025\ k_B$K and $E_S^{\mathrm{qu}} = 830\ k_B$K.

Sometimes, however, quantum effects can be so strong that phenomena occur which have no classical analogue. Those phenomena are often related to tunnelling or coherence. A well-known example is the ground state of solid H_2, which is an orientationally disordered hcp crystal in the case of para-H_2 and a fully ordered fcc crystal in the case of ortho-H_2 [139].

The purpose of path integral simulations is to include the quantum fluctuations *rigorously* in the computer simulation. Thus, given a well-defined model and Hamiltonian, PIMC simulation for rotational degrees of freedom leads to a *numerically exact* quantification of rotational quantum effects without further approximations. This is the main distinguishing feature of PIMC simulation compared to approximate treatments of rotational degrees of freedom, such as mean-field [43, 86, 146, 147], quasi-classical [47, 48, 71, 88, 89, 97, 147], or quasi-harmonic [16, 53, 54, 88, 89, 97] approximations. However, the quasi-analytical methods can lead to more easily gained and deeper insight into the physics that governs a particular system [146, 147]. In the following subsections, a few selected examples of using PIMC methods in condensed matter physics will be discussed. In addition, these applications serve as demonstrations of various aspects of the theory outlined in section 2.

3.1. Rotor impurities

3.1.1. The Devonshire model. Simple systems such as one-particle systems are usually best suited for studying the prospects and limitations of a given numerical method. At the same time, understanding the physics of one-particle models often helps in interpreting the behaviour of more complex systems. A simple generic model potential for describing two-dimensional rotor impurities ($d^{\mathrm{rot}} = 2$) in solids, e.g., the solid mixture of cubic $\mathrm{Ar}_{1-x}(\mathrm{N}_2)_x$ with $x \ll 1$, has been proposed by Devonshire [128]. The interaction potential with strength $\propto \mathcal{J}$ reads

$$V = \frac{3}{2}\mathcal{J}(1 - e_1^4 - e_2^4 - e_3^4) \tag{3.1}$$

where (e_1, e_2, e_3) denotes the normalized vector indicating the molecule's orientation. The Devonshire model focuses on the coupling of the orientational degrees of freedom to the crystal field V_{CF}, which stems from atoms sitting at cubic lattice sites. It neglects translation–rotation coupling V_{TR} [81], which quantifies the change of energy due to centre-of-mass displacements away from cubic lattice sites. The coupling between orientational degrees of freedom—the so-called rotation–rotation coupling V_{RR} [81]—is not considered either, due to the absence of direct rotor–rotor interactions in the limit $x \ll 1$. It is worth mentioning that MFT of diluted and undiluted molecular solids maps V_{RR} onto V_{CF}, whose parameters are then obtained self-consistently as a function of temperature. Therefore, single-particle models may even be interpreted as effectively describing many-rotor interactions. This is the case in particular in an ordered phase far away from the critical point, where MFT often turns out to be a reasonable approximation.

A feature incorporated in the Devonshire model is tunnelling, which becomes important at low temperatures in nearly all molecular solids. Tunnelling can occur if the corresponding classical system has a ground state that is at least twofold degenerate [39,75,137]. The quantum mechanical system removes the degeneracy by allowing for coherent angular motion between the wells in which the classical ground states can be found. In analogy to the case for other multi-well potentials [39, 75, 137], one may expect that the smaller the ratio $\mathcal{J}/B$ of energy barriers $\mathcal{J}$ to the rotational constant B (2.21) the larger the tunnelling splitting $\hbar\omega_{\mathrm{T}}$. Simulating this motion between the various wells with PIMC simulation is often CPU time consuming, because a typical realization of a path has to explore all wells. This may only be possible if a time step $\Delta\tau = \hbar\beta/P$ in the order of—or small compared to—the barrier $\mathcal{J}$ is chosen. Sufficiently small values for $\Delta\tau$ therefore have to be much smaller at low temperatures than at temperatures where the system may already be strongly quantum mechanical but does not yet show coherent tunnelling.

An interesting property of the Devonshire model is that for rotational constants $B^\star = B/\mathcal{J} < 1/40$, two anomalies in the specific heat can be observed. One maximum occurs when the rotor crosses over from librations within the wells to the free-rotor regime. The latter regime can be found at thermal energies similar to or larger than the barrier. Another maximum in the specific heat occurs due to the onset of quantum mechanical coherence at $T^\star \approx 0.007$ for $B^\star = 1/40$; see figure 4 in [109]. Between these two maxima, two regimes might be expected: one regime in which the rotor behaves like a classical oscillator and another one in which the rotor is quantum mechanically frozen in. However, $B^\star = 1/40$ is not yet small enough to allow for the above-mentioned classical regime, even though it appears to be a small value. Hence, extreme care has to be taken when rotors are meant to behave classically. For example, $\mathrm{Ar}_{1-x}(\mathrm{N}_2)_x$ is often referred to as a classical system. However, realistic simulations at zero pressure show an energy barrier of 70 k_{B}K [107], which translates to $B^\star \approx 1/20$ if mapped onto the Devonshire model. Thus, quantum fluctuations cannot be neglected if the aim of the simulation is a *quantitative* investigation of this and related systems.

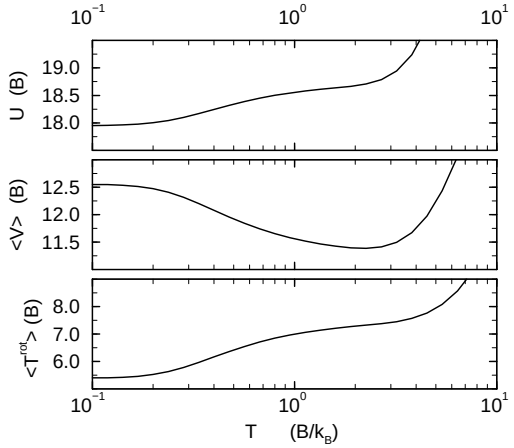

Figure 6. The internal energy U and expectation values $\langle V\rangle$ and $\langle T^{\rm rot}\rangle$ of the potential and kinetic energy, respectively, for the Devonshire model as defined in (3.1) using a barrier height of $\mathcal{J} = 40B$. All energies are expressed in units of the rotational constant B. Adapted from [109].

An important property of the Devonshire model as well as of most multi-well models is that in the regime $0 < k_{\rm B}T < \mathcal{O}\{\hbar\omega_{\rm T}\}$ the average potential energy $\langle V\rangle$ may decrease as the temperature increases, in contrast to the kinetic energy and total energy which both increase. This behaviour is shown in figure 6 for the same Devonshire model as was discussed above, namely that with $\mathcal{J} = 40B$. This means that *thermal fluctuations can lead to localization* by destroying quantum coherence. This mechanism may be responsible for some interesting characteristics of the so-called QAPR model; see section 3.2.1. In the QAPR model the order parameter *increases* with temperature in a certain regime of rotational constants and temperatures; see section 3.2.1.

3.1.2. Hydrogen molecules on ice. Simulations of realistic models include PIMC studies of H_2 on amorphous ice clusters [12, 13]. Restricting the angular momentum to $J = 0$ (and thus $M = 0$) for para-H_2 and to $J = 1$ (and thus $M = -1, 0, 1$) for ortho-H_2, a PIMC approach was chosen that is similar in spirit to the one introduced in [56]. It was found that ortho-H_2 couples more strongly to the ice cluster than para-H_2 [12]. This can again be understood in terms of coherence. If the Hilbert space of the rotor can be decomposed into at least two symmetry classes, the quantum mechanical ground state will be found in the identity representation. To be specific, para-H_2 and ortho-D_2 are in the identity representation while ortho-H_2 and para-D_2 are not. As shown as an example in section 3.1.1, the ground-state energy is minimized due to coherent tunnelling between equivalent potential energy wells, which reduces the kinetic energy. However, the quantum mechanical ground state does not have the lowest possible potential energy! Other representations have nodes in their wave functions. Hence they are more localized, and the coupling to external potentials is stronger. Using a self-consistent field approximation together with an adiabatic approximation, it is possible to extend the Hilbert space of the rotational degrees of freedom and to obtain a semi-quantitative agreement with an experimentally observed rotational spectrum of H_2 on amorphous ice; see figure 1 in [13]. These results are certainly encouraging given the complexity of the system, in particular the H_2–H_2O and H_2O–H_2O interactions. However, the approach used to simulate the rotational degrees of freedom can hardly be extended rigorously if many rotors interact directly, for the reasons mentioned in the last paragraph of section 2.1.

Nevertheless, it was possible to generalize this approach to several interacting rotors in the limit of sufficiently weak anisotropic potentials in conjunction with an approximate diagonalization scheme in a truncated rotational Hilbert space. See [14] for the detailed formulation of this method. The aforementioned allows the simulation of mixed para-D_2/ortho-D_2 clusters consisting of up to 13 molecules based on using electric quadrupole–quadrupole interactions (3.6) to represent the anisotropic interactions. An exact diagonalization was still possible for up to five odd-J para-D_2 molecules. An interesting result was that at 1 K the three odd-J molecules of the (para-D_2)$_3$(ortho-D_2)$_{10}$ cluster 'form a cluster within the cluster'. At 3 K, however, they are 'dissolved' throughout the entire cluster. The three central molecules are found to be held together by the EQQ interactions. A similar phase separation at low temperatures was discovered for mixed para-H_2/ortho-D_2 clusters consisting of 18 spherically symmetric even-J molecules modelled by a fused-atom Lennard-Jones interaction [23, 24]. In this case, the segregation is induced by the mass difference that leads to stronger delocalization of the lighter para-H_2 molecules. Therefore they concentrate at the cluster 'surface' where the potential is the shallowest and the zero-point energy is minimal. The (para-D_2)$_{13}$ cluster consisting of only odd-J molecules shows some local orientational order at 1 K due to the quadrupolar interactions that favour T-shaped arrangements for linear molecules [14]. However, a perfectly ordered ground state cannot be reached because of a geometrical frustration effect.

3.2. Rotors on surfaces

3.2.1. The QAPR model and quantum melting. A generic model for the description of rotational ordering of linear molecules in bulk phases, or physisorbed on surfaces [98], is the anisotropic planar rotor (APR) model [117, 118]. It focuses on the description of one-dimensional rotors, $d^{\mathrm{rot}} = 1$, pinned onto a triangular lattice and constrained to rotate in a common plane. Next-neighbour rotors within the plane interact through the corresponding anisotropic part of their electric quadrupoles. The APR model is ideally suited to describe the transition from the so-called herringbone phase to an orientationally disordered phase on a triangular lattice [98]. However, it can easily be modified or generalized, and applied to the description of a large variety of problems such as coupled Josephson junctions [63–65], polymers on surfaces [29], and spherical impurities in an extended array of rotors [28, 54, 114].

In this review we focus on the quantum mechanical generalization of the APR model, the quantum anisotropic planar rotor (QAPR) model introduced in [92, 97]. The parameters of its Hamiltonian $\hat{H}_{\mathrm{QAPR}}$ are the rotational constant B and the coupling strength $\mathcal{J}$:

$$\hat{H}_{\mathrm{QAPR}} = -B \sum_{i=1}^{N} \frac{\partial^2}{\partial \varphi_i^2} + \mathcal{J} \sum_{\langle i,j \rangle} \cos(2\varphi_i + 2\varphi_j - 4\phi_{i,j}) \tag{3.2}$$

with $\varphi_i = \varphi(\boldsymbol{R}_i)$ the angle of the ith molecule pinned at lattice site $\boldsymbol{R}_i$, and $\phi_{i,j}$ the six phases that measure the angle relative to the vector that connects the neighbouring sites $\boldsymbol{R}_i$ and $\boldsymbol{R}_j$; all angles are defined relative to a given space-fixed axis. The discrete positions $\boldsymbol{R}_i$ are the vertices of a periodically replicated rigid triangular lattice. The QAPR model reduces to the classical APR in the limit $B = 0$. The order parameter that is sensitive to the herringbone structure [106] follows from the three-component order parameter (Φ_1, Φ_2, Φ_3) and is given by

$$\Phi = \left[\sum_{\alpha=1}^{3} \Phi_\alpha^2 \right]^{1/2} \tag{3.3}$$

with

$$\Phi_\alpha = \frac{1}{N}\sum_{i=1}^{N} \sin(2\varphi_i - 2\eta_\alpha)\exp(\mathrm{i}\boldsymbol{Q}_\alpha \cdot \boldsymbol{R}_i) \tag{3.4}$$

and

$$\begin{aligned} \boldsymbol{Q}_1 &= 2\pi(0, 2/\sqrt{3}) & \eta_1 &= 0 \\ \boldsymbol{Q}_2 &= 2\pi(-1, -1/\sqrt{3}) & \eta_2 &= 2\pi/3 \\ \boldsymbol{Q}_3 &= 2\pi(1, -1/\sqrt{3}) & \eta_3 &= 4\pi/3. \end{aligned} \tag{3.5}$$

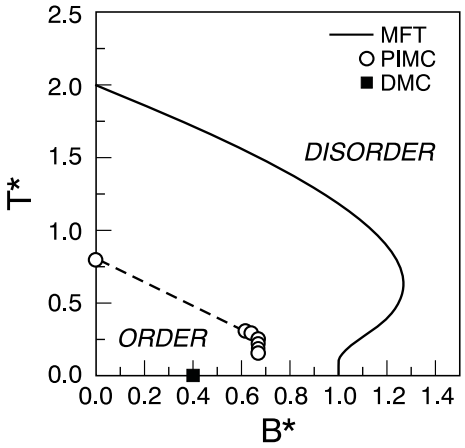

Figure 7. Phase diagram of the QAPR model (3.2) as a function of the reduced temperature $T^\star = k_\mathrm{B}T/\mathcal{J}$ and the reduced rotational constant $B^\star = B/\mathcal{J}$. Mean-field theory (MFT): solid curve; path integral Monte Carlo simulations (PIMC): open circles (the dashed line connects the data linearly); diffusion Monte Carlo simulations (DMC): filled square. Adapted from [86, 112].

One of the interesting features of the QAPR model is that MFT predicts a re-entrant behaviour in the B–T plane [86]; see the solid curve in figure 7. Similarly, re-entrance was predicted by MFT for related molecular solids [11, 43–46]. It is still under debate whether an approximation-free treatment of the QAPR model would lead to re-entrance or not.

In the $B^\star$–$T^\star$ phase diagram ($B^\star = B/\mathcal{J}$, $T^\star = k_\mathrm{B}T/\mathcal{J}$) depicted in figure 7, several distinct regimes can be found as revealed by various simulation studies [59, 86, 92, 97]; see the key. For all values of $B^\star$ the system is disordered at high temperatures. However, the transition temperatures $T^\star(B^\star)$ are reduced compared to the classical transition temperature $T^\star_\mathrm{cl} = T^\star(B^\star = 0) = 0.76$ [93, 116]. For values $B^\star \lesssim 0.69$ a temperature-driven transition from the high-temperature disordered phase to an orientationally ordered phase can be found with $T^\star(B^\star = 0.69) \approx 0.3$. The order parameter (3.3) can reach its maximum value of unity only in the classical zero-temperature limit, i.e., exactly for $B^\star = 0$, whereas quantum fluctuations always reduce the maximum value—in particular $\Phi(T^\star = 0) < 1$ for every $B^\star > 0$; see figure 3 of [97]. A similar behaviour, which is mainly induced by zero-point motion in the potential wells, was observed for realistic models of N_2 [88,89] and CO [90,91] molecules physisorbed on graphite. See section 3.2.2 for a deeper discussion of this phenomenon. No long-range orientational order seems possible for $B^\star \gtrsim 0.69$ at any temperature [86, 97], i.e., $\Phi(T^\star \gtrsim 0.69) = 0$. In the vicinity of $B^\star = 0.69$, a sharp drop in $T^\star(B^\star)$ as a function of increasing $B^\star$ has been observed [97]. First, finite-size studies did not provide indications of re-entrance and were inconclusive [86]. However, more recent PIMC studies [59] based on

Cao's method [18]—see section 2.2.2—in conjunction with finite-size scaling show evidence for re-entrance at $B^\star = 0.6364$. The system orders upon cooling at $T^\star \approx 0.25$. Upon further cooling, the Binder cumulant [7] (i.e., the reduced fourth moment of the order parameter, which is an indicator for phase transitions) suddenly drops at $T^\star \approx 0.09$ for all system sizes studied, indicating a disordered phase for $T^\star \lesssim 0.09$. Re-entrance also receives support from a ground-state $T^\star = 0$ diffusion Monte Carlo study [112], in which the zero-temperature quantum melting is roughly located at $B^\star \approx 0.4$, which is substantially lower than $B^\star \approx 0.69$ at $T^\star(B^\star = 0.69) \approx 0.3$ (compare the square (DMC) to the circles (PIMC) in figure 7).

Given the present data, it may be convenient to distinguish between the following regimes as a function of the reduced rotational constant $B^\star$ (see also figure 3 of [97]):

(i) The 'classical regime', $B^\star = 0$, in which the orientational order parameter Φ (3.3) is unity at zero temperature, $\Phi(T^\star = 0) = 1$, and a monotonically decreasing function of increasing temperature.

(ii) The 'quasi-classical regime', $0 < B^\star \lesssim 0.4$, with an ordered ground state, $0 < \Phi(T^\star = 0) < 1$, and the possibility of an order parameter growing with *increasing* temperature in a certain temperature interval before the order parameter decays to zero for high temperatures.

(iii) The 're-entrance regime', $0.4 \lesssim B^\star \lesssim 0.69$, for which the ground state is disordered, $\Phi(T^\star = 0) = 0$, whereas thermal destruction of quantum coherence leads to ordering in a finite temperature interval $\Delta T^\star$, $0 < \Phi(\Delta T^\star) < 1$, before further heating produces the high-temperature disordered phase with $\Phi(T^\star \to \infty) = 0$.

(iv) The 'quantum regime' $B^\star \gtrsim 0.69$ in which the system is a quantum orientational liquid, i.e., disordered at all temperatures with $\Phi(T^\star \geqslant 0) = 0$.

Note that the present classification differs slightly from that proposed in [97].

Unfortunately, the experimental realizations of the QAPR model can only be found in either the quasi-classical regime (N_2 or CO on graphite; see section 3.2.2) or in the quantum mechanical regime (H_2 on graphite, where, however, the $d^{\mathrm{rot}} = 1$ approximation for diatomic molecules is no longer satisfactory). However, the QAPR model might nevertheless be helpful in understanding why there is re-entrance in solid HD under pressure, but not in solid H_2 and D_2 [105]. In addition, over the years the APR model acquired the status of the 'Ising model for rotations' and thus merits a thorough quantum statistical investigation of its phase diagram in its own right.

3.2.2. N_2 and CO on graphite. The investigation of the phases and associated phase transitions of diatomics physisorbed on surfaces is a vast field of research [98]. In a series of publications, the impact of quantum effects on the orientational ordering of diatomics on graphite was investigated by PIMC methods [87–92]. The aim was to provide a model that is as realistic as possible, but still efficient enough to allow for the study of quantum effects on phase transitions. To this end, the rigid rotors were pinned with their centres of mass on a triangular lattice corresponding to the so-called $(\sqrt{3} \times \sqrt{3})\mathrm{R}30^\circ$ commensurate superstructure on the graphite basal plane. The molecule–molecule and molecule–surface interactions were both treated in microscopic detail using atomistic site–site models in conjunction with point charges in order to represent multipole–multipole electrostatic interactions. This allowed us to treat 900 interacting quantum molecules, which is a sufficiently large system to lead to meaningful conclusions for collective phenomena.

In the case of N_2 on graphite, the ground state is known to possess so-called '2-in' herringbone orientational order, where the molecular axes are coplanar with the surface with only minor out-of-plane fluctuations [98]. Thus, a one-dimensional $d^{\mathrm{rot}} = 1$ approximation

for this diatomic rotor is realistic. In addition, the rotational constant of N_2 is small enough to allow for an unconstrained (no-spin) summation over all rotational levels according to (2.27)—compare the no-spin approximation to the quenched or annealed averages in figure 3. This would be a less satisfactory approximation for H_2 as demonstrated in figure 4, where the different averaging procedures (annealed, quenched, and no-spin; see section 2.5 and in particular section 2.5.1) affect the physics.

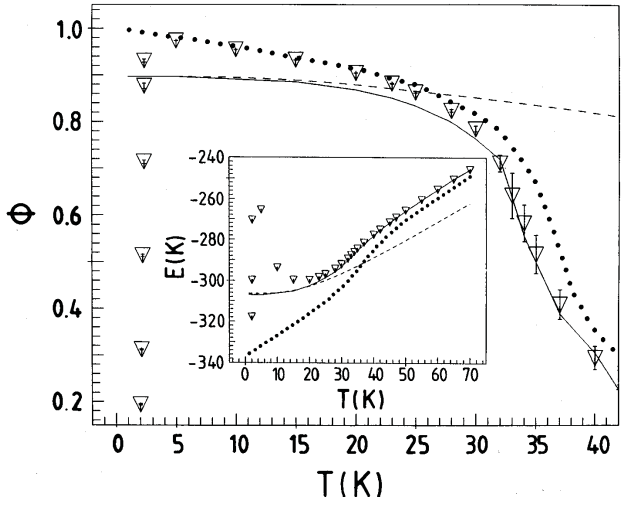

Figure 8. The herringbone order parameter Φ (3.3) and total energy E (inset) from PIMC simulations of 900-rigid-rotor $d^{\mathrm{rot}} = 1$ N_2 molecules physisorbed on graphite at a function of temperature. Solid curve: PIMC simulation; dotted curve: classical simulation; dashed curve: quasi-harmonic approximation; triangles: quasi-classical Feynman–Hibbs approximation; the curves are linear connections of the data. Adapted from [88].

One of the main results of the study of N_2 on graphite is that quantum fluctuations lead to '10% effects' on physical properties [88, 89]. In particular, it is found that temperature of the transition to the herringbone phase is shifted by about 10% to lower temperatures as a result of zero-point motion. This means that a quantitative agreement between experiment and theory cannot be expected if quantum effects are neglected in the theoretical modelling. The order parameter (3.3) in the ground state is also reduced by about 10% due to quantum librations of the rotors in the potential wells—compare the solid (quantum) to the dotted (classical) curve in the main panel of figure 8. Thus, the order parameter does not reach its classical value of unity at $T = 0$ K, but only about $\Phi(T = 0\ \mathrm{K}) \approx 0.9$.

It is instructive to compare this order parameter reduction to the behaviour of a model that is related in spirit, namely the spin-1/2 quantum Heisenberg model on a two-dimensional rigid lattice. In the ferromagnetic case, the quantum order parameter is known to reach its classical Curie value of unity in the ground state. This is qualitatively different for the antiferromagnetic case where the staggered order parameter is reduced from its classical Néel value by about 40% on a square lattice [130]. The reduction on the honeycomb lattice is even as large as approximately 60% [131]. Despite this unusual behaviour of the quantum *anti*ferromagnetic Heisenberg model, it was shown that the nature of the order parameter and the scenario of ordering by spontaneous symmetry breaking is the same as for the analogous classical model [132]. The reason for the fundamentally different behaviour of the ferromagnetic and antiferromagnetic cases is that for the former the order parameter operator commutes with

the Hamiltonian, whereas this is not true for antiferromagnetic interactions. The situation for the herringbone ordering is similar to that of the antiferromagnetic model because the order parameter (3.3) does not commute with the Hamiltonian, even for the simplified QAPR model (3.2). The difference is of course that the non-commutativity in the antiferromagnetic Heisenberg model stems exclusively from the interaction term, whereas it is the kinetic energy term that leads to this phenomenon in the rotor models. Thus, the order parameter reduction in the Heisenberg case is a constant for a given lattice symmetry, but it is a mass-dependent effect for rotors.

Monolayers of the heteropolar CO molecules physisorbed on graphite have one additional degree of freedom compared to homopolar N_2. Their molecular dipole moments lead to head–tail order (within a quadrupolar ordered structure of the herringbone type) at very low temperatures [61,162], which is *not* found in the bulk phase. It was shown experimentally [162] and theoretically [90,91] that the head–tail ordering transition belongs to the two-dimensional Ising universality class. The lowering of the head–tail transition temperature due to quantum fluctuations was again found to amount to roughly 10%, whereas the depression of the ground state head–tail order parameter is quite small [90, 91]. Incidentally, the herringbone order parameter reduction in the ground state was found to be less pronounced for CO than for N_2 on graphite, although the rotational constants are very similar ($B_{\mathrm{CO}} = 2.8\ k_{\mathrm{B}}\mathrm{K}$ versus $B_{\mathrm{N}_2} = 2.9\ k_{\mathrm{B}}\mathrm{K}$).

With the realistic example of heavy diatomics on graphite at hand, it was also checked how well approximate methods such as quasi-harmonic theory or quasi-classical approaches of the Feynman–Hibbs type (see section 2.2.4) work [88]; see [89] for further details. It was confirmed that they work very well in the low- and high-temperature limits, respectively, as demonstrated in figure 8 for the N_2 herringbone order parameter and the total energy. However, there is an intermediate temperature window were *both* methods start to fail. In addition, these methods are shown to break down for lighter molecules, even at quite low and high temperatures, respectively [97]. Furthermore, because MFT grossly overestimates the transition temperature by a factor of *at least* two (see, e.g., figure 7), the numerical PIMC method is the only reliable and quantitative technique left for studying orientational ordering of interacting quantum rotors at finite temperatures.

3.3. Rotors in the bulk

3.3.1. Solid molecular hydrogen. Investigating the structure of solid molecular hydrogen as a function of pressure and temperature has been an active field of research for many decades [139]. More recently, the focus of attention, both experimentally and theoretically, has shifted from the low-pressure regime to higher pressures, i.e., up to the order of 1 Mbar or 100 GPa [85]. Among the interesting phenomena is a pressure-induced orientational ordering phase transition of the even-J species, which occur for ortho-D_2 and para-H_2 in the low-temperature limit at approximately 30 GPa and 110 GPa, respectively. The orientationally disordered low-pressure phase is called the symmetric phase (SP) or phase I, whereas the ordered high-pressure phase is dubbed the broken-symmetry phase (BSP) or phase II. A phase transition to a third phase, the H-A phase or phase III, occurs at even higher pressure of approximately 150 GPa for low temperatures. A model approach that can be used to rationalize these orientational transitions can be found in [45, 46, 100]. The odd-J species, i.e., para-D_2 and ortho-H_2, have an ordered ground state already at zero applied pressure.

A pioneering PIMC rotor simulation of the pressure-induced order–disorder transition between phases I and II was based on a $d^{\mathrm{rot}} = 2$ rigid-rotor model of even-J homopolar diatomics that were pinned with their centres of mass on a rigid fcc lattice [133, 148]. Thus,

lattice vibrations (phonons) and intramolecular vibrations (vibrons) were neglected from the outset. In a more realistic PIMC simulation along the same lines, phonons were taken into account, pressure was an observable in the constant-pressure ensemble employed, and the interactions were adjusted to reproduce the experimental equation of state [31]. In [133], the expression (2.39) was evaluated numerically, taking into account only the even-J contributions with $J \leqslant 50$, and tabulated on a grid as a function of the relative angle α between the rotors. An effective anisotropic pair potential was determined by fitting to energies obtained by density functional electronic structure calculations performed in the local density approximation. Furthermore, the realistic assumption was made that the nuclear spin state of the molecules does not change, i.e., the quenched averaging procedure for a pure even-J sample was used; see section 2.5 and (2.52).

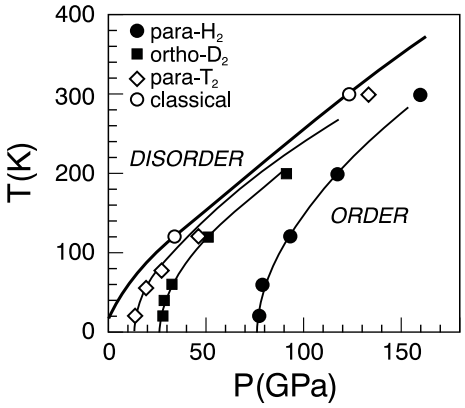

Figure 9. The phase diagram from PIMC simulations of $d^{\mathrm{rot}} = 2$ rigid-rotor even-J homopolar hydrogen isotopomers on a rigid fcc lattice as a function of temperature and pressure. Filled circles: para-H_2; filled squares: ortho-D_2; open diamonds: para-T_2; open circles: classical molecules; the curves are to guide the eye. Adapted from [133].

The resulting phase diagrams [133] for various isotopomers are reproduced in figure 9. In the zero-temperature limit the order–disorder transitions are located at around $p_0 \approx 75.0$ GPa for para-H_2, 26.4 GPa for ortho-D_2, and 12.3 GPa for para-T_2. Classical rotors with the same interaction potential are, of course, orientationally ordered already at zero applied pressure. Thus, quantum fluctuations in the orientational degrees of freedom destroy long-range orientational order if no external pressure is applied. The lighter the nuclei, the higher the external pressure has to be in order to induce orientational ordering, as one can see from the increasing transition pressure p_0 with increasing rotational constant. This is in agreement with experimental trends. In addition, the transition pressure is found to depend sensitively on the symmetry of the underlying rigid lattice. A hcp lattice leads to much higher order–disorder transition pressures of $p_0 \approx 120$ GPa for para-H_2 and 49 GPa for ortho-D_2.

Orientational ordering was also investigated using a simplified $d^{\mathrm{rot}} = 1$ rigid-rotor model for H_2 molecules with centres of mass fixed on a rigid hcp lattice [72]. Because the one-dimensional rotors were constrained to in-plane rotation, the resulting phases were called azimuthally ordered and disordered phases. This is also why the associated phase transition cannot be unambiguously related to either the I–II or the II–III orientational transition. It is argued that releasing the constraint on the second rotational degree of freedom would lead to a shift of the order–disorder transition to higher pressures and lower temperatures. Nuclear spin was not taken into account, i.e. the no-spin approximation as discussed in section 2.5 and

in particular in section 2.5.1 was invoked. It is, however, unclear how the path integration of the one-dimensional rotational degrees of freedom was performed—in particular, whether the summation over winding numbers was included (explicitly or implicitly). Taking into account only the $n = 0$ term would lead to an artificial suppression of quantum effects; see our discussion at the end of section 2.2.3. In the present case it would result in an underestimation of transition pressures.

The markedly different orientational ordering scenarios of the odd-J fermionic diatomic homopolar para- and ortho-species were investigated on the basis of a model consisting of $N = 108$ electric quadrupoles on a rigid fcc lattice [124]. The corresponding Hamiltonian can be written symbolically as

$$\hat{H}_{\mathrm{EQQ}} = -B \sum_{i=1}^{N} \left(\frac{\partial^2}{\partial \vartheta_i^2} + \cot\vartheta_i \, \frac{\partial}{\partial \vartheta_i} + \frac{1}{\sin^2 \vartheta_i} \, \frac{\partial^2}{\partial \varphi_i^2} \right) + \frac{Q^2}{r_0^2} \sum_{\langle i,j \rangle} V_{\mathrm{EQQ}}(\Omega_i, \Omega_j) \tag{3.6}$$

where Q denotes the electric quadrupole moment, r_0 is nearest-neighbour distance on the fcc lattice, $B = \hbar^2/2\Theta$ is the rotational constant, and $\Omega_i = (\vartheta_i, \varphi_i)$. The explicit definition of the angular dependence of the EQQ interactions V_{EQQ} is given, e.g., in equation (2.1) in [84]. The fixed-node approximation was used to treat the odd-J fermionic case; see section 2.5.2 for a presentation of this method.

The ground state for the even-J species is the spherically symmetric $J = 0$ state. Thus, the $J = 2$ or higher levels have to be populated in order to destroy spherical symmetry and to produce orientational ordering. In the limit of weak quadrupolar interactions the system can stay in the $J = 0$ state. For strong quadrupolar interactions, however, the potential energy can only be lowered at the expense of increasing the kinetic energy by populating $J > 0$ levels, which leads to orientational ordering. Because the strength of quadrupolar interactions increases with decreasing intermolecular distance, $\propto Q^2/r_0^5$, orientational ordering of even-J species can be achieved by compressing the system, i.e., by increasing the external pressure; see the discussion of figure 9 above. For odd-J species, in contrast, the $J = 1$ ground state has a threefold-degenerate anisotropy that can always be broken independently of pressure by lowering the temperature.

In addition to temperature, there are two parameters present: the strength of EQQ interactions $\propto Q^2/r_0^5$ and the magnitude of the rotational constant B. Thus, two variables that are reduced by the strength of the quadrupolar interactions can be defined: the dimensionless temperature $T^\star = k_{\mathrm{B}} T r_0^5/Q^2$ and the dimensionless rotational constant $B^\star = B r_0^5/Q^2$; for H_2 and D_2 at zero pressure, $B^\star \approx 5$ and 2, respectively. The resulting phase diagram of (3.6) is shown in figure 10. In the classical limit (i.e., for $B^\star = 0$) there is no difference between the para- and ortho-species, and their order–disorder transitions occur at the same temperature of about $T^\star \approx 0.72$, which is of course overestimated by MFT ($T^\star \approx 1.18$). The ground state (i.e., for $T^\star = 0$) of the even-J species is only orientationally ordered in the limit of sufficiently small quantum fluctuations, more precisely if $B^\star < 0.30 \pm 0.01$ (with MFT predicting $B^\star < 0.40$). Contrary to that, the phase transition line for the odd-J species is almost independent of the rotational constant for $B^\star > 1$ and its ground state is always ordered, independently of $B^\star$. In particular, the odd-J system is ordered in the regime $T^\star \lesssim 0.14$ in the limit $B^\star \to \infty$ (with MFT predicting $T^\star \lesssim 0.45$).

Interestingly, a re-entrant phase boundary is found if *all* rotational J-levels are included in the determination of the density matrix within MFT [124]; see also [45,46]. This can serve as a model for HD molecules where both nuclei are distinguishable and thus no symmetry restriction for the rotational density matrix applies. The re-entrance can be rationalized *qualitatively* by the fact that the ground state of the rotor is again the isotropic $J = 0$ state, but the first excited (anisotropic) level is $J = 1$ and thus much closer to the ground state than the $J = 2$ state,

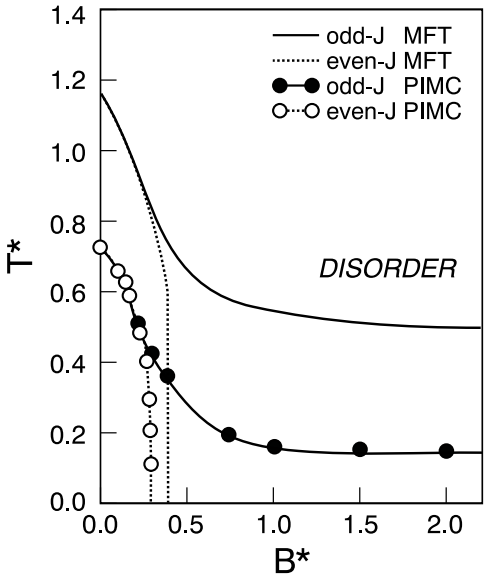

Figure 10. The phase diagram of $d^{\mathrm{rot}} = 2$ rigid quadrupoles on a rigid fcc lattice as a function of the dimensionless temperature $T^\star = k_{\mathrm{B}}Tr_0^5/Q^2$ and the dimensionless rotational constant $B^\star = Br_0^5/Q^2$. Solid curve: odd-J species MFT; dashed curve: even-J species MFT. Filled circles: odd-J species PIMC simulation; open circles: even-J species PIMC simulation; here the connecting thin curves are to guide the eye. The orientationally ordered phases are found on the lower left-hand side of the various separating curves. Adapted from [124].

which is the first excited state for even-J species. Thus, it is possible that for certain values of the rotational constant $B^\star$ the system is orientationally disordered in the ground state at $T^\star = 0$, orders upon increasing temperature because of mixing in the $J = 1$ state, and finally disorders again as thermal fluctuations become dominant. This all-J behaviour would result in a bump in the curve for the even-J case in figure 10 similar to the case for the MFT curve shown in figure 7. Note that re-entrance is, in principle, also possible for even-J species as the same arguments apply, which means that re-entrance is the result of a delicate balance between the magnitude of the rotational constant and the strength and possibly the symmetry of the interactions. As discussed in section 3.2.1, MFT also predicts for the QAPR model a re-entrant regime in the phase diagram for heteronuclear $d^{\mathrm{rot}} = 1$ diatomics (or in general within the no-spin approximation), but a final consensus as regards what happens beyond MFT is not yet reached, although it seems that more recent simulations support the idea of re-entrance. Finally, we mention again that re-entrance is also found in experiments with HD at high pressures [105].

3.3.2. Solid methane. Cubic solid methane (CH_4) at atmospheric pressures is an interesting system due to its peculiar ground state and its strong isotope effects [128]. The ground-state lattice can be decomposed into two sublattices, one of which is orientationally ordered, while the other is orientationally disordered [66]. The transition from the plastic phase to the partially orientationally ordered phase is a first-order transition taking place at a temperature $T_1(CH_4) = 20.4$ K [127]. A similar transition takes place in cubic CD_4 at a higher temperature $T_1(CD_4) = 27.4$ K [126]. In addition, CD_4 transforms into a fully ordered solid upon further cooling [83].

Using a model potential based on *ab initio* results and a no-spin free-particle kernel, transition temperatures $T_1(CH_4) = 16$ K and $T_1(CD_4) = 23$ K were found within a PIMC study [110]. It is worth noting that near the transition point T_1, CH_4 is almost quantum mechanically frozen and a small shift in the potential invokes a large shift in the thermal properties. This effect might be responsible for the relatively large discrepancy between simulation and experiment. However, the relative shift in T_1, due to the use of different isotopes, has been reproduced satisfactorily.

The effects of the rotational wave function's symmetry on the transition temperature were investigated in this study as well. Two different kernels were used in the simulations. The no-spin kernel, which neglects exchange effects stemming from the nuclei, and the kernel in the identity representation, which contains, among other states, the ground state. Using the identity representation, a reduction of $\Delta T_1 = 6$ K was found with respect to the no-spin result. This effect may make possible the observation of an inverse hysteresis at a first-order phase transition. If CH_4 were cooled down from high temperatures to well below T_1 fast enough to prevent the nuclear degrees of freedom from thermalizing, it would be appropriate to mimic this experiment by using an annealed kernel or alternatively a no-spin kernel. In this case, a transition temperature $T_1^{\mathrm{no-spin}}(CH_4) = 16$ K would be expected. If the system were tempered at low temperatures long enough to thermalize the nuclear degrees of freedom, practically all molecules would convert and occupy the ground state in the identity representation. This coherent state is more delocalized than a ground state in any other representations [165]. Upon a fast re-heating, the transition to a disordered state can then be expected to be found at $T_1^{\mathrm{no-spin}}(CH_4) = 10$ K, which is lower than $T_1^{\mathrm{no-spin}}(CH_4)$. This scenario corresponds to an inverse hysteresis.

3.3.3. Liquid water. The definite determination of the structure of liquid water as characterized by, e.g., radial distribution functions, is still controversial [140]. Among many questions are those related to the quantum nature of the molecules in the condensed phase. This is of particular interest because one important technique for extracting partial (i.e., atom–atom) radial distribution functions from the measured total structure factor is the so-called isotopic substitution technique. This approach relies on the assumption that different isotopomers (in the case of water H_2O, HDO, and D_2O) have a very similar (or even an identical) microscopic structure. In order to shed light on this issue, several computer simulations of 'quantum' liquid water were carried out, beginning in the mid-eighties. In most cases, flexible water models were used. Here, we focus on rigid models where the rotations are treated explicitly using path integrals.

A method for coping with *rigid* models representing water molecules was developed and used in [32, 77, 78] to study liquid water at ambient conditions. The rotations of the rigid bodies were quantized using the approach presented in (2.48) and (2.49). The influence of treating the centre-of-mass motion classically or quantum mechanically in conjunction with quantum rotations was also assessed. Simulations for light (H_2O) and heavy (D_2O) liquid water were initially carried out with the so-called ST2 model of water [77, 78] and later complemented with calculations based on the SPC and TIP4P models [32]; see the original articles for details and references. A discretization parameter as small as $P = 3$ or 5 was judged to be satisfactory for quantizing the rotations for a small test case, an isolated water dimer at room temperature. The simulations were carried out with 125 or 100 water molecules subject to periodic boundary conditions.

The observables of prime interest in such simulations are radial distribution functions. A general result is, as expected, that the classical liquid is the most structured, light water is the

least structured, and heavy water is in between. Thus, the maxima decrease and the minima increase in height, and both shift to larger distances as the system becomes more quantum mechanical. These effects are even manifest in the oxygen–oxygen radial distribution function, and not only in the partial radial distribution functions that involve the much lighter H or D atoms. In addition, the heavier the nuclei the smaller the librational motion. This leads to more linear hydrogen bonds ($HO–H\cdots OH_2$) between the water molecules for classical water compared to light water. The structural quantum effects could be attributed mainly to the orientational degrees of freedom rather than the centre-of-mass motion of the rigid bodies. Furthermore, it was found that changes in structural properties in going from classical to quantum water were roughly comparable to the changes which accompany a 50 K temperature increase of the liquid [78]. Viewed this way, one can conclude that the quantum effects on the structure of liquid water at ambient conditions are not that small.

4. Concluding remarks

What has been achieved? We started this journey by decomposing the partition function of a many-rigid-body system into centre-of-mass translation, rigid-body rotation, and interaction contributions by making use of Trotter's theorem. Thereby, the problem was reduced to a well-known one, the path integral treatment of interacting point particles, and the evaluation of a high-temperature rotational density matrix. Depending on the number of rotational degrees of freedom involved, different strategies for the computation of the rotational contribution can be chosen. For two- or three-dimensional rotation the density matrix is best evaluated in advance by performing the summations over rotational quantum numbers explicitly. The result is tabulated as a function of relative angle for later use in the simulation. The one-dimensional case is somewhat special, since the summation over the rotational levels has to be done by Monte Carlo sampling. These techniques not only work in principle, but also in practice. Most PIMC and related simulations carried out in the framework of rotational degrees of freedom deal with the question by how much the results of classical simulations have to be corrected if quantum fluctuations are taken into account. These corrections often reduce the discrepancy between simulation and experiment by an order of magnitude. Impressive examples can be found in particular for adsorbed monolayers, clusters, and solids. Thus, the path integral simulation technique of rigid molecules is a mature field.

What remains to be done? A problem that deserves further attention is the inclusion of anti-symmetry or intramolecular exchange of indistinguishable nuclei. This manifests itself most prominently in the coupling of nuclear spins to rotations, which is the basis for the distinct behaviour of the ortho- and para-species of diatomics at low temperatures. No systematic study is known to us that shows how accurate the fixed-node approximation is. Another problem to be solved is how to apply efficient sampling algorithms such as staging to two- and three-dimensional rotation. This is particularly important for simulations at low temperatures, where the use of large Trotter numbers easily leads to a critical slowing down. Molecular systems at thermal energies well below the rotational constant, however, often reveal interesting physical phenomena due to the crossover from de-coherence to coherence. These phenomena are purely quantum mechanical and do not have classical analogues. One of the distinctly challenging problems in this context is certainly the simulation of the low-temperature specific heat anomaly in disordered molecular crystals. The simulation of those systems may shed light on the microscopic mechanisms of collective tunnelling in disordered media at low temperatures. Thus, despite impressive progress, there is ample room for future developments!

Acknowledgments

Much of our knowledge on the subject covered in this review has slowly grown in pleasant collaborations with Bruce Berne, Kurt Binder, Balazs Hetenyi, Roman Martoňák, Peter Nielaba, and Surajit Sengupta, which we take this opportunity to gratefully acknowledge.

References

[1] Allen M P and Tildesley D J 1987 *Computer Simulation of Liquids* (Oxford: Clarendon)
[2] Allen M P 1988 *CCP5* (Information quarterly for computer simulation of condensed phases) **29** 26
[3] Barker J A 1979 *J. Chem. Phys.* **70** 2914
[4] Bellman R 1961 *A Brief Introduction to Theta Functions* (New York: Holt, Rinehart and Winston)
[5] Benoit M, Marx D and Parrinello M 1998 *Nature* **392** 258
[6] Berne B J and Thirumalai D 1986 *Annu. Rev. Phys. Chem.* **37** 401
[7] Binder K 1981 *Z. Phys.* B **43** 119
[8] Binder K (ed) 1986 *Monte Carlo Methods in Statistical Physics* (Berlin: Springer)
[9] Binder K and Heermann D W 1988 *Monte Carlo Simulation in Statistical Physics* (Berlin: Springer)
[10] Binder K and Ciccotti G (ed) 1996 *Monte Carlo and Molecular Dynamics of Condensed Matter Systems* (Bologna: Società Italiana di Fisica and Editrice Compositori)
[11] Brodyanskii A P, Sumarokov V V, Freiman Yu A and Jezowski A 1993 *Low Temp. Phys.* **19** 368
[12] Buch V and Devlin J P 1993 *J. Chem. Phys.* **98** 4195
[13] Buch V, Silva S C and Devlin J P 1993 *J. Chem. Phys.* **99** 2265
[14] Buch V 1994 *J. Chem. Phys.* **100** 7610
[15] Burton W K and De Borde A H 1955 *Nuovo Cimmento* **2** 197
[16] Cahill J E and Leroi G E 1969 *J. Chem. Phys.* **51** 97
[17] Cao J and Berne B J 1992 *J. Chem. Phys.* **97** 2382
[18] Cao J 1994 *Phys. Rev.* E **49** 882
[19] Ceperley D and Alder B 1986 *Science* **231** 555
[20] Ceperley D M 1991 *J. Stat. Phys.* **63** 1237
[21] Ceperley D M 1995 *Rev. Mod. Phys.* **67** 279
For errata and udpates see: `http://www.ncsa.uiuc.edu/Apps/CMP/papers/cep95a/cep95a.html`.
[22] Ceperley D M 1996 *Monte Carlo and Molecular Dynamics of Condensed Matter Systems* ed K Binder and G Ciccotti (Bologna: Società Italiana di Fisica and Editrice Compositori)
[23] Chakravarty Ch 1995 *Phys. Rev. Lett.* **75** 1727
[24] Chakravarty Ch 1996 *J. Chem. Phys.* **104** 7223
[25] Chakravarty Ch 1997 *Int. Rev. Phys. Chem.* **16** 421
[26] Chandler D and Wolynes P G 1981 *J. Chem. Phys.* **74** 4078
[27] Chandler D 1991 *Liquids, Freezing and Glass Transition* ed J P Hansen, D Levesque and J Zinn-Justin (Amsterdam: North-Holland)
[28] Choi H-Y and Mele E J 1989 *Phys. Rev.* B **40** 3439
[29] Choi H-Y, Harris A B and Mele E J 1989 *Phys. Rev.* B **40** 3766
[30] Cuccoli A, Macchi A, Pedrolli G, Tognetti V and Vaia R 1995 *Phys. Rev.* B **51** 12 369
[31] Cui T, Cheng E, Alder B J and Whaley K B 1997 *Phys. Rev.* B **55** 12 253
[32] Del Buono G S, Rossky P J and Schnitker J 1991 *J. Chem. Phys.* **95** 3728
[33] De Raedt H and De Raedt B 1983 *Phys. Rev.* A **28** 3575
[34] De Raedt H and Frick M 1993 *Phys. Rep.* **231** 107
[35] Doll J D and Gubernatis J E (ed) 1990 *Quantum Simulations of Condensed Matter Phenomena* (Singapore: World Scientific)
[36] Edwards S F and Gulyaev Y V 1964 *Proc. R. Soc.* A **279** 229
[37] Ermakova E, Solca J, Huber H and Marx D 1995 *Chem. Phys. Lett.* **246** 204
[38] Fernandes P A, Carvalho A P and Ramalho J P P 1995 *J. Chem. Phys.* **103** 5720
[39] Feynman R P and Hibbs A R 1965 *Quantum Mechanics and Path Integrals* (New York: McGraw-Hill)
[40] Feynman R P 1972 *Statistical Mechanics: A Set of Lectures* (Redwood City, CA: Addison-Wesley)
[41] Fosdick L D 1962 *J. Math. Phys.* **3** 1251
[42] Fosdick L D and Jordan H F 1966 *Phys. Rev.* **143** 58
[43] Freiman Yu A, Sumarokov V V, Brodyanskii A P and Jezowski A 1991 *J. Phys.: Condens. Matter* **3** 3855
[44] Freiman Yu A, Tretyak S and Jezowski A 1998 *J. Low Temp. Phys.* **110** 147

[45] Freiman Yu A, Tretyak S and Jezowski A 1998 *J. Low Temp. Phys.* **111** 475
[46] Freiman Yu A, Tretyak, S M, Jezowski A and Hemley R J 1998 *Low Temp. Phys.* **24** 518
[47] Friedmann J 1962 *Adv. Chem. Phys.* **4** 225 (see [48] for generalizations)
[48] Friedmann J 1963 *Physica* **30** 921
[49] Fye R M 1986 *Phys. Rev.* B **33** 6271
[50] Fye R M 1986 *J. Stat. Phys.* **43** 827
[51] Fye R M and Scalettar R T 1987 *Phys. Rev.* B **36** 3833
[52] Gillan M J 1990 *Computer Modelling of Fluids Polymers and Solids* ed C R A Catlow, S C Parker and M P Allen (Dordrecht: Kluwer)
[53] Goodings D A and Henkelman M 1971 *Can. J. Phys.* **49** 2898
[54] Harris A B, Mouritsen O G and Berlinsky A J 1984 *Can. J. Phys.* **62** 915
[55] Hama J and Miyagi H 1973 *Prog. Theor. Phys.* **50** 1142
[56] Helbing W, Nielaba P and Binder K 1991 *Phys. Rev.* B **44** 4200
[57] Herman M F, Bruskin E J and Berne B J 1982 *J. Chem. Phys.* **76** 5150
[58] Herzberg G 1945 *Infrared and Raman Spectra of Polyatomic Molecules (Molecular Spectra and Molecular Structure II)* (New York: Van Nostrand Reinhold)
[59] Hetenyi B, Müser M H, Ankerhold J and Berne B J 1999 in preparation
[60] Ilisca E 1991 *Mod. Phys. Lett.* B **5** 1191
[61] Inaba A, Shirakami T and Chihara H 1988 *Chem. Phys. Lett.* **146** 63
[62] Inui T, Tanabe Y and Onodera Y 1996 *Group Theory and Its Applications in Physics* (Berlin: Springer)
[63] Jacobs L, José J V and Novotny M A 1984 *Phys. Rev. Lett.* **53** 2177
[64] Jacobs L, José J V, Novotny M A and Goldman A M 1987 *Europhys. Lett.* **3** 1295
[65] Jacobs L, José J V, Novotny M A and Goldman A M 1988 *Phys. Rev.* B **38** 4562
[66] James H M and Keenan T A 1959 *J. Chem. Phys.* **31** 12
[67] Janke W and Kleinert H 1979 *Nuovo Cimento Lett.* **25** 297
[68] Janke W and Sauer T 1996 *Chem. Phys. Lett.* **263** 488
[69] Jordan H F and Fosdick 1968 *Phys. Rev.* **171** 128
[70] José J V, Kadanoff L P, Kirkpatrick S and Nelson D R 1977 *Phys. Rev.* B **16** 1217
José J V, Kadanoff L P, Kirkpatrick S and Nelson D R 1978 *Phys. Rev.* B **17** 1477 (erratum)
[71] José J V 1984 *Phys. Rev.* B **29** 2836
[72] Kaxiras E and Guo Z 1994 *Phys. Rev.* B **49** 11 822
[73] Kilpatrick J E, Fukuda Y and Larsen S Y 1965 *J. Chem. Phys.* **43** 430
[74] Kirkwood J G 1933 *Phys. Rev.* **44** 31
[75] Kleinert H 1990 *Path Integrals in Quantum Mechanics, Statistics and Polymer Physics* (Singapore: World Scientific)
[76] Krauth W 1996 *Phys. Rev. Lett.* **77** 3695
[77] Kuharski R A and Rossky P J 1984 *Chem. Phys. Lett.* **103** 357
[78] Kuharski R A and Rossky P J 1985 *J. Chem. Phys.* **82** 5164
[79] Li X-P and Broughton J Q 1987 *J. Chem. Phys.* **86** 5094
[80] Loh E Y Jr, Gubernatis J E, Scalettar R T, White S R, Scalapino D J and Sugar R L 1990 *Phys. Rev.* B **41** 9301
[81] Lynden-Bell R M and Michel K H 1994 *Rev. Mod. Phys.* **66** 721
[82] Magro W R, Ceperley D M, Pierleoni C and Bernu B 1996 *Phys. Rev. Lett.* **76** 1240
[83] Maki K, Kataoka Y and Yamamoto T 1979 *J. Chem. Phys.* **70** 655
[84] Mandell M J 1974 *J. Chem. Phys.* **60** 1432
[85] Mao H-k and Hemley R J 1994 *Rev. Mod. Phys.* **66** 671
[86] Martoňák R, Marx D and Nielaba P 1997 *Phys. Rev.* E **55** 2184
[87] Marx D and Nielaba P 1992 *Phys. Rev.* A **45** 8968
[88] Marx D, Opitz O, Nielaba P and Binder K 1993 *Phys. Rev. Lett.* **70** 2908
[89] Marx D, Sengupta S and Nielaba P 1993 *J. Chem. Phys.* **99** 6031
[90] Marx D, Sengupta S, Nielaba P and Binder K 1994 *Phys. Rev. Lett.* **72** 262
[91] Marx D, Sengupta S, Nielaba P and Binder K 1994 *Surf. Sci.* **321** 195
[92] Marx D, Sengupta S and Nielaba P 1994 *Ber. Bunsenges. Phys. Chem.* **98** 525
[93] Marx D, Sengupta S, Opitz O, Nielaba P and Binder K 1994 *Mol. Phys.* **83** 31
[94] Marx D 1994 *Mol. Simul.* **12** 33
[95] Marx D and Parrinello M 1994 *Z. Phys.* B **95** 143 (Rapid Note)
[96] Marx D and Parrinello M 1995 *Nature* **375** 216
[97] Marx D and Nielaba P 1995 *J. Chem. Phys.* **102** 4538
[98] Marx D and Wiechert H 1996 *Adv. Chem. Phys.* **95** 213

[99] Marx D and Parrinello M 1996 *J. Chem. Phys.* **104** 4077
[100] Mazin I I, Hemley R J, Goncharov A F, Hanfland M and Mao H-k 1997 *Phys. Rev. Lett.* **78** 1066
[101] McDowell R S 1990 *J. Chem. Phys.* **93** 2801
[102] McQuarrie D A 1976 *Statistical Mechanics* (New York: Harper and Row)
[103] Miller W H 1971 *J. Chem. Phys.* **55** 3146
[104] Morita T 1973 *J. Phys. Soc. Japan* **35** 980
[105] Moshary F, Chen N H and Silvera I F 1993 *Phys. Rev. Lett.* **71** 3814
[106] Mouritsen O G and Berlinsky A J 1982 *Phys. Rev. Lett.* **48** 181
[107] Müser M H, Helbing W, Nielaba P and Binder K 1994 *Phys. Rev.* E **49** 3956
[108] Müser M H, Nielaba P and Binder K 1995 *Phys. Rev.* B **51** 2723
[109] Müser M H 1996 *Mol. Simul.* **17** 131
[110] Müser M H and Berne B J 1996 *Phys. Rev. Lett.* **77** 2638
[111] Müser M H and Berne B J 1997 *J. Chem. Phys.* **107** 571
[112] Müser M H and Ankerhold J 1998 *Europhys. Lett.* **44** 216
[113] Neumann M and Zoppi M 1989 *Phys. Rev.* A **40** 4572
[114] Nicol E J C, Kallin C and Berlinsky A J 1988 *Phys. Rev.* B **38** 556
[115] Nielaba P and Binder K 1990 *Europhys. Lett.* **13** 327
[116] Opitz O, Marx D, Sengupta S, Nielaba P and Binder K 1993 *Surf. Sci. Lett.* **297** L122
[117] O'Shea S F and Klein M L 1979 *Chem. Phys. Lett.* **66** 381
[118] O'Shea S F and Klein M L 1982 *Phys. Rev.* B **25** 5882
[119] Parrinello M and Rahman A 1984 *J. Chem. Phys.* **80** 860
[120] Pauling L 1930 *Phys. Rev.* **36** 430
[121] Peak D and Inomata A 1969 *J. Math. Phys.* **10** 1422
[122] Pierleoni C, Ceperley D M, Bernu B and Magro W R 1994 *Phys. Rev. Lett.* **73** 2145
[123] Pollock E L and Ceperley D M 1984 *Phys. Rev.* B **30** 2555
[124] Pollock E L and Runge K J 1994 *Physica* B **197** 180
[125] Presber M, Löding D, Martoňák R and Nielaba P 1998 *Phys. Rev.* B **58** 11 937
[126] Press W 1972 *J. Chem. Phys.* **56** 2597
[127] Press W and Kollmar A 1975 *Solid State Commun.* **17** 405
[128] Press W 1981 *Single-Particle Rotations in Molecular Crystals* (Berlin: Springer)
[129] Rau A R P 1992 *Rev. Mod. Phys.* **64** 623
[130] Reger J D and Young A P 1988 *Phys. Rev.* B **37** 5978
[131] Reger J D, Riera J A and Young A P 1989 *J. Phys.: Condens. Matter* **1** 1855
[132] Reger J D 1991 *J. Physique* II **1** 259
[133] Runge K J, Surh M P, Mailhiot C and Pollock E L 1992 *Phys. Rev. Lett.* **69** 3527
Runge K J, Surh M P, Mailhiot C and Pollock E L 1993 *Phys. Rev. Lett.* **70** 2974 (addendum)
[134] Savit R 1980 *Rev. Mod. Phys.* **52** 453
[135] Schmidt K E and Ceperley D M 1992 *The Monte Carlo Method in Condensed Matter Physics* ed K Binder (Berlin: Springer)
[136] Schulman L 1968 *Phys. Rev.* **176** 1558
[137] Schulman L S 1981 *Techniques and Applications of Path Integrations* (New York: Wiley)
[138] Sesé L M 1993 *Mol. Phys.* **78** 1167
[139] Silvera I F 1980 *Rev. Mod. Phys.* **52** 393
[140] Soper A K 1997 *J. Phys.: Condens. Matter* **9** 2717
[141] Sorella S, Baroni S, Car R and Parrinello M 1989 *Europhys. Lett.* **8** 663
[142] Sprik M, Klein M L and Chandler D 1985 *Phys. Rev.* B **31** 4234
[143] Stern T E 1931 *Proc. R. Soc.* A **130** 551
[144] Stratt R M 1979 *J. Chem. Phys.* **70** 3630
[145] Stratt R M 1980 *J. Chem. Phys.* **72** 1685
[146] Stratt R M 1985 *Phys. Rev. Lett.* **55** 1443
[147] Stratt R M 1986 *J. Chem. Phys.* **84** 2315
[148] Surh M P, Runge K J, Barbee T W III, Pollock E L and Mailhiot C 1997 *Phys. Rev.* B **55** 11 330
[149] Suzuki M 1976 *Prog. Theor. Phys.* **56** 1454
[150] Suzuki M 1976 *Commun. Math. Phys.* **51** 183
[151] Suzuki M, Miyashita S and Kuroda A 1977 *Prog. Theor. Phys.* **58** 1377
[152] Suzuki M 1986 *J. Stat. Phys.* **43** 883
[153] Suzuki M 1987 *Quantum Monte Carlo Methods in Equilibrium and Nonequilibrium Systems* ed M Suzuki (Berlin: Springer)

[154] Takahashi M and Imada M 1984 *J. Phys. Soc. Japan* **53** 3765
[155] Thirumalai D, Hall R W and Berne B J 1984 *J. Chem. Phys.* **81** 2523
[156] Tinkham M 1972 *Group Theory and Quantum Mechanics* (New York: McGraw-Hill)
[157] Trotter H F 1959 *Proc. Am. Math. Soc.* **10** 545
[158] Tuckerman M E, Berne B J, Martyna G J and Klein M L 1993 *J. Chem. Phys.* **99** 2796
[159] Tuckerman M E, Marx D, Klein M L and Parrinello M 1996 *J. Chem. Phys.* **104** 5579
[160] Tuckerman M E and Hughes A 1998 *Classical and Quantum Dynamics in Condensed Phase Simulations* ed Berne B J, Ciccotti G and Coker D F (Singapore: World Scientific)
[161] Villain J 1975 *J. Physique* **36** 581
[162] Wiechert H and Arlt St-A 1993 *Phys. Rev. Lett.* **71** 2090
[163] Wigner E 1932 *Phys. Rev.* **40** 749
[164] Wilson Jr E B, Decius J C and Cross P C 1980 *Molecular Vibrations—The Theory of Infrared and Raman Vibrational Spectra* (New York: Dover)
[165] Yamamoto T, Kataoka Y and Okada K 1977 *J. Chem. Phys.* **66** 2701
[166] Zare R N 1988 *Angular Momentum* (New York: Wiley)